



Copyright Undertaking

This thesis is protected by copyright, with all rights reserved.

By reading and using the thesis, the reader understands and agrees to the following terms:

1. The reader will abide by the rules and legal ordinances governing copyright regarding the use of the thesis.
2. The reader will use the thesis for the purpose of research or private study only and not for distribution or further reproduction or any other purpose.
3. The reader agrees to indemnify and hold the University harmless from and against any loss, damage, cost, liability or expenses arising from copyright infringement or unauthorized usage.

IMPORTANT

If you have reasons to believe that any materials in this thesis are deemed not suitable to be distributed in this form, or a copyright owner having difficulty with the material being included in our database, please contact lbsys@polyu.edu.hk providing details. The Library will look into your claim and consider taking remedial action upon receipt of the written requests.

**OPTICAL AND ELECTRICAL PROPERTIES OF
TWO-DIMENSIONAL MATERIALS**

TAN CHOON KIAT

M.Phil

The Hong Kong Polytechnic University

2018



The Hong Kong Polytechnic University

Department of Applied Physics

**Optical and Electrical Properties of
Two-Dimensional Materials**

Tan Choon Kiat

A thesis submitted in partial fulfillment of the requirements

for the degree of Master of Philosophy

June 2017



Certificate of Originality

I hereby declare that this thesis is my own work and that, to the best of my knowledge and belief, it reproduces no material previously published or written, nor material that has been accepted for the award of any other degree or diploma, except where due acknowledgement has been made in the text.

_____ (Signature)

TAN Choon Kiat (Name of candidate)



Abstract

Two-dimensional (2D) materials provide an ideal platform for the study of fundamental properties of system with atomic-level thickness. These studies motivate a large number of device application in various fields, for example, electronics and display technology. After the first discovery of remarkable properties such as high impermeability, large heat and electrical conductivity etc., of 2D carbon sheet known as graphene, other layered materials including transition metal dichalcogenides (TMD) have been widely investigated. These TMD possess a sizable bandgap that is very promising for future optical and electronic devices. However, other 2D family groups such as 2D layered superconductor and p-n junctions formed by 2D materials still remain relatively unexplored.

In this thesis, firstly, we characterized the basic properties of 2D iron-based superconductor. This study shows that the thickness of exfoliated FeTe is correlated to its number of layers, similar to other TMD materials. The effect of the layer thickness on the Raman spectra have been measured. As the number of layers goes down to few layers, the separation of the Raman peaks A_{1g} and E_{2g}^1 decreases. Furthermore, the superconductivity in the exfoliated FeTe and FeSe has been studied. The temperature dependent resistances were measured and structural transition sometimes could be observed.

Secondly, Raman spectra of encapsulated bulk and few layers MoS₂ in multiple uniaxial strain direction have been measured. A modified bending technique has been employed to apply precise uniaxial tensile strain along different directions of MoS₂ which was encapsulated in between octadecagon polyethylene terephthalate (PET) and a layer



of polymethylmethacrylate (PMMA). For bulk MoS₂, the Raman shift rates of the E_{2g}¹ and A_{1g} mode (the change of the Raman peak position versus strain level) are almost the same for strains applied along different directions. The Raman shift rates of few layers MoS₂, on the other hand, are larger than those in bulk MoS₂. In addition, they also exhibit distinctive anisotropic strain responses. We believe that the Armchair and Zigzag directions of the exfoliated MoS₂ might be determined by monitoring the variation of Raman Shift of the E_{2g}¹ and A_{1g} modes in different strained direction of MoS₂.

Lastly, the Raman spectroscopic study of the effect of electrode preparation on the structural properties of As₂S₃ has been carried out. As₂S₃ is an intrinsic p-type semiconductor with a melting point around 310 °C. Electrode preparation involving E-beam lithography and E-beam evaporation, might result heating on the samples. Raman spectra have been measured before and after the two above mentioned processes. Raman spectra of As₂S₃ before and after the processes are indicating that the electrode preparation does not influence the As_sS₃. Furthermore, p-type As₂S₃ and n-type MoS₂ have been used to study the p-n junction behaviour in 2D materials. Current-Voltage (I-V) curves were measured under various circumstances such as low temperature and illuminating under white light. IV curves of As₂S₃ and PN junction showed high resistance which might due to the low mobility in As_sS₃ (10⁻¹⁰ cm²/Vs)



List of publications

1. **Tan, C.K.**, Wong, W. C., Ng, S. M., Mak, C. L., & Leung, C. W. (2017). Raman spectra in different strain directions of MoS₂, IEEE EDSSC



Acknowledgement

This M.Phil. study has been carried out for the past two years at The Hong Kong Polytechnic University and it has been one of the most important periods in my life. Many people have been giving me helps, guidance and support throughout my entire study. I would like to express my deep appreciation to those people.

First of all, I would like to express my sincerest appreciation and thank to my supervisor, Dr. MAK Chee Leung and co-supervisor Dr. LEUNG Chi Wah for their enthusiastic encouragement and enlightening advice throughout the past two years. Without their excellent guidance, and constant support, it would be impossible for me to complete my study.

I would also like to thank the technicians who supported me in my study: Dr. W. Lu for his help in E-beam lithography; Dr. Hardy Lu for his guidance in MRC facility; Dr. Terence Wong for his guidance in Clean room facility. an Mr. W.F. Cheng for his valuable time on writing the LabVIEW programs.

Furthermore, I would like to thank all the group members and colleagues for their great help and friendship, including Mr. K.H. Chan, Mr. K.K. Lam, Mr. W.H. Fung, Mr. H.F. Ting, Mr. K.F. Lee and Mr. Hilton Tam. I would like to acknowledge my special thanks to Mr. W.C. Wong, Ms. Theresa Ng and Mr. H.F. Wong for their assistance, motivation and encouragement throughout my study.

Last but not least, I would like to express my deep love and cordial thanks to my parents and Ms. K.L. Lim for their endless support and love throughout my life. They have been supporting me at every moment.



Finally, I would also like to thank the financial support from of the Hong Kong Polytechnic University which is very essential for me and my study.



Table of Contents

Certificate of Originality	iii
Abstract	iv
List of publications.....	vi
Acknowledgement.....	vii
Table of Contents	ix
List of Figures	xii
List of Tables.....	xvii
1. Introduction	1
1.1. Introduction of two-dimensional materials	1
1.2. Property of 2D materials	5
1.2.1. Molybdenum disulphide (MoS_2).....	5
1.2.2. Iron Selenide (FeSe).....	10
1.2.3. Iron Telluride (FeTe).....	11
1.2.4. Arsenic Trisulfide (As_2S_3).....	12
1.3. Literature review	13
1.3.1. Strain Effect on MoS_2 by Raman Spectroscopy	13
1.3.2. P-N junction in 2D materials	13



1.3.3.	Superconductivity in Iron-Based 2D materials	15
1.4.	Objective of research	16
1.5.	Outline of thesis.....	17
2.	Methodology	19
2.1.	Substrate patterning and Sample Fabrication Methods	19
2.1.1.	Photolithography	19
2.1.2.	Magnetron Sputtering.....	20
2.1.3.	Electron beam Evaporation	23
2.1.4.	Mechanical Exfoliation	25
2.1.5.	Dry Transfer	25
2.2.	Characterization techniques.....	27
2.2.1.	Atomic force microscopy (AFM).....	27
2.2.2.	Raman spectroscopy.....	29
2.2.3.	Two-point & Four-point measurement	32
3.	Optical properties of 2-Dimensional Materials.....	37
3.1.	Preparation of MoS ₂ and FeTe	37
3.1.1.	MoS ₂	37
3.1.2.	FeTe.....	41
3.2.	Raman Spectra in different strained direction of MoS ₂	42
3.3.	Raman Spectra for different thicknesses of FeTe.....	50
3.4.	Summary	53



4. Electrical properties of 2-dimensional Materials	55
4.1. Experimental Setup	55
4.2. Effect of Electrode Preparation process on As_2S_3	58
4.3. Study of I-V characteristic of P-N junction.....	61
4.4. Superconductivity in Iron-Based 2D materials	65
4.3.1. Iron Telluride (FeTe).....	65
4.3.2. Iron Selenide (FeSe).....	67
4.4. Summary	69
5. Conclusion and Future Work	71
5.1. Conclusion.....	71
5.2. Future work	73
Reference.....	74

List of Figures

Figure 1.1 Various types of 2D materials from insulator to superconductor. E_g denotes the band gap from ref. [12]	2
Figure 1.2: Timeline of Superconductor from Ref. [29].....	4
Figure 1.3 Crystal structure of MoS ₂ . (a) Chemical structure of two layers of MoS ₂ . (b) Two polytypes of single layer MoS ₂ : trigonal prismatic (1H) and octahedral (1T). (c) Schematic illustration of the two typical Raman active phonon modes (E_{2g}1 and A_{1g}) from Ref.[39].....	6
Figure 1.4 Raman characterizations of sample S2 using 532 nm line. The Raman spectra of different locations with various thicknesses on sample S2. Inset: optical image of sample S2. The left and right dashed lines indicate the positions of the and peaks in bulk MoS ₂ , respectively. The scale bars represent 2 μ m. “1 L”, “2 L”, “3 L”, “4 L”, and “5 L” indicate monolayer, bilayer, trilayer, quadrilayer, and quinquelayer, respectively from ref. [42].....	7
Figure 1.5 Layer dependence of photoluminescence efficiency in MoS ₂ . (a) Photoluminescence and Raman spectra of MoS ₂ monolayer, bilayer, hexalayer, and bulk sample. Different Raman peaks can be assigned to the MoS ₂ and silicon vibration modes. For MoS ₂ thin layers, monolayer MoS ₂ Raman signal is relatively weak because less material is being excited. However, photoluminescence is the strongest in monolayer MoS ₂ in spite of reduced material. (b) Photoluminescence spectra normalized by Raman intensity for MoS ₂ layers with different thickness, showing a dramatic increase of luminescence efficiency in MoS ₂ monolayer from ref. [42, 43].....	9
Figure 1.6 Crystal structure of FeSe from ref. [47].....	10



Figure 1.7 Characterizations of atomically thin FeTe samples. (a) Three-dimensional representation of the structure of FeTe. Single layers, 11.1 Å thick. (b) Tetragonal structure of FeTe from ref. [49, 50] 11

Figure 1.8 Structure of As₂S₃ from ref. [57] 12

Figure 2.1 UV contact aligner 20

Figure 2.2 (a) Schematic diagram of the D.C magnetron sputtering system (b) The experimental setup of the D.C. magnetron sputtering system used in this work. 22

Figure 2.3 Schematic Diagram of Electron Beam Evaporation from ref. [93] 24

Figure 2.4 Electron Beam Evaporation 24

Figure 2.5 (a) SEM image of tri-layer graphene on the surface of the viscoelastic stamp (b) SEM image of tri-layer graphene transferred onto hexagonal boron nitride from ref. [95] 26

Figure 2.6 XYZ stage together with optical microscope for dry transfer 27

Figure 2.7 (a) Principle of AFM (b) schematic of AFM from ref. [96] 28

Figure 2.8 Atomic force microscopy 29

Figure 2.9 Schematic diagram of Raman scattering from ref. [98] 30

Figure 2.10 Raman spectroscopy 32

Figure 2.11 Two-wire resistance measurement configuration 32

Figure 2.12 (a) Two-point IV characterize curve measurement configuration (b) The experimental setup of Two-point IV characterize curve measurement 34

Figure 2.13 Four-point resistance measurement configuration 35

Figure 2.14 Physical Property Measurement System 36

Figure 3.1 PET with octadecagon shape 38

Figure 3.2 Schematic diagram of PET with octadecagon shape 39



Figure 3.3 Schematic diagrams showing the fabrication process of MoS₂ encapsulated in between SU-8 and PMMA on PET substrate (a-b) Spin coating of SU-8 (c) Baking process (d) Transferring MoS₂ on top of PET (e) Spin coating of PMMA (f) Baking process (Not drawn to scale)..... 39

Figure 3.4 Moulds built by 3D printer 40

Figure 3.5 PET substrate embedded in between 3D mould..... 41

Figure 3.6 Optical image of the encapsulated bulk MoS₂ on PET substrate without applied uniaxial strain..... 42

Figure 3.7 Optical image of the encapsulated quadrilayer MoS₂ on PET substrate without applied uniaxial strain 42

Figure 3.8 Raman spectra of the encapsulated quadrilayer MoS₂ on PET substrate without applied uniaxial strain 43

Figure 3.9 Raman shift of **E2g1** modes of the bulk MoS₂ as a function of the applied strain for different uniaxial strain directions together with linear fitting..... 44

Figure 3.10 Raman shift of A_{1g} modes of the bulk MoS₂ as a function of the applied strain for different uniaxial strain directions together with linear fitting..... 45

Figure 3.11 Raman shift of **E2g1** modes of the quadrilayer MoS₂ as a function of the applied strain for different uniaxial strain directions together with linear fitting..... 47

Figure 3.12 Raman shift of A_{1g} modes of the quadrilayer MoS₂ as a function of the applied strain for different uniaxial strain directions together with linear fitting..... 48

Figure 3.13 Basic Raman Study of FeTe. (a) Optical image of bulk FeTe (b) Raman spectra of bulk FeTe..... 51

Figure 3.14 Optical images of thin FeTe. (a) Optical image of thin FeTe (b) AFM image (c) Optical image of thin FeTe (d) AFM image..... 52



Figure 3.15 Characterization of thin FeTe. (a) step height measurement of the thin FeTe (b) step height measurement of another thin FeTe (c) Raman spectra of thin FeTe (d) Graph of Thickness of FeTe against peak separation. 52

Figure 4.1 Silicon Substrate Alignment Mark 56

Figure 4.2 (a) Optical image of Original As_2S_3 (b) Optical image of As_2S_3 after E-Beam Lithography (c) Optical image of As_2S_3 after E-beam Evaporation (d) Raman spectra with respect to original, part cover under PMMA, part after E-Beam Lithography, part cover by gold and without gold of As_2S_3 58

Figure 4.3 (a) Optical image of Original As_2S_3 (b) Optical image of As_2S_3 under Raman microscopy (c) Optical image of As_2S_3 after E-beam lithography (d) Raman spectra with respect to before and after E-Beam Lithography. 60

Figure 4.4 Optical image of PN junction formed by As_2S_3 and MoS_2 61

Figure 4.5 (a) Raman Spectra of As_2S_3 and MoS_2 (b) I-V characteristic curve of MoS_2 (c) I-V characteristic curve of As_2S_3 (d) I-V characteristic curve of p-n junction 62

Figure 4.6 (a) I-V characteristic response of As_2S_3 exposed to white LED (b) I-V characteristic response of p-n junction exposed to white LED 64

Figure 4.7 (a) Structural diagram of FeTe sample (b) Enlargement of Raman Spectrum from 1000 to 3000 cm^{-1} (c) Enlargement of Raman Spectrum from 100 to 300 cm^{-1} (d) Raman Spectrum of FeTe after covered by Graphene..... 65

Figure 4.8 Temperature dependence of resistance for FeTe together with the enlargement image of the low temperature part 66

Figure 4.9 (a) Structural diagram of FeSe sample covered by PMMA (b) Temperature dependence of resistance for FeSe covered by PMMA (c) Structure of FeSe sample without PMMA (d) Temperature dependence of resistance for FeSe..... 68

Figure 4.10 Bad contact for FeSe with gold electrodes below 77K..... 69





List of Tables

Table 1 Summary of the **E2g1** and A_{1g} peak frequencies measured by a 488nm laser. “1 L”, “2 L”, “3 L”, and “4 L” indicate monolayer, bilayer, trilayer, and quadrilayer, respectively. A single data represents the average value from three different samples from ref. [42]..... 8

Table 2 Raman shift rate of **E2g1** modes of the bulk MoS_2 for different uniaxial strain directions 44

Table 3 Raman shift rate of A_{1g} modes of the bulk MoS_2 for different uniaxial strain directions 45

Table 4 Raman shift rate of **E2g1** modes of the quadrilayer MoS_2 for different uniaxial strain directions 47

Table 5 Raman shift rate of A_{1g} modes of the quadrilayer MoS_2 for different uniaxial strain directions 48



1. Introduction

1.1. Introduction of two-dimensional materials

Since the discovery of remarkable properties of two-dimensional (2D) sheets of carbon known as graphene[1], 2D materials experienced a glowing age since it was the very first mechanically exfoliated material from three-dimensional (3D) graphite in 2004 [1]. Monolayer graphene possesses some highlighted properties, such as high electrical conductivity ($\sim 10^4 \Omega^{-1} \text{cm}^{-1}$), high thermal conductivity at room temperature ($3 \times 10^3 \text{W/mK}$), high Young's modulus (1.1 TPa) and high transparency [2, 3]. However, the zero or low band gap character of graphene do not favour the development towards electronic and optical devices[4].

The discovery of graphene has sparked researchers' interest in other graphene-like 2D materials aiming at broadening the range of application and the shortage of graphene [3]. Scientists, then, focus on other 2D materials such as transition metal dichalcogenides (TMD) with a general chemical formula of MX_2 ($\text{M}=\text{Mo}, \text{W}$; $\text{X}=\text{S}, \text{Se}, \text{Te}$) which exhibit distinctive electronic and optical properties[5, 6]. For example, the crystal structure of molybdenite monolayers was already studied in 1923 by Dickinson and Pauling [7] and in 2014 monolayer MoS_2 was investigated again[8]. These layered materials have layered structure with strong in-plane ionic bond/covalent bonds within layers and weak van der Waals (vdW) coupling between layers [9, 10]. As a result, layered materials can be exfoliated and the number of layers can be reduced down to monolayers. With reduced dimension, the physical properties of such materials change drastically. For example, the electronic states of tungsten disulphide (WS_2) shift from indirect bandgap at bulk to direct

bandgap of $\sim 2.05\text{eV}$ in monolayer[11]. Single-crystalline WS_2 grown by sulphurizing WO_3 films showed extraordinary photoluminescence between 1.99 and 1.94 eV at different positions of the sample, which is dependent on thickness[11]. Generally speaking, layered materials can be categorized into different family groups based on their chemical formula, such as graphene family, 2D oxides and 2D dichalcogenides, or based on their electrical properties, such as insulators (BN , HfS_2), semiconductors (GaSe , GaS , CuS), semi-metals (graphene) and superconductors (NbSe_2 , FeSe , FeTe) as shown in Figure 1.1 .

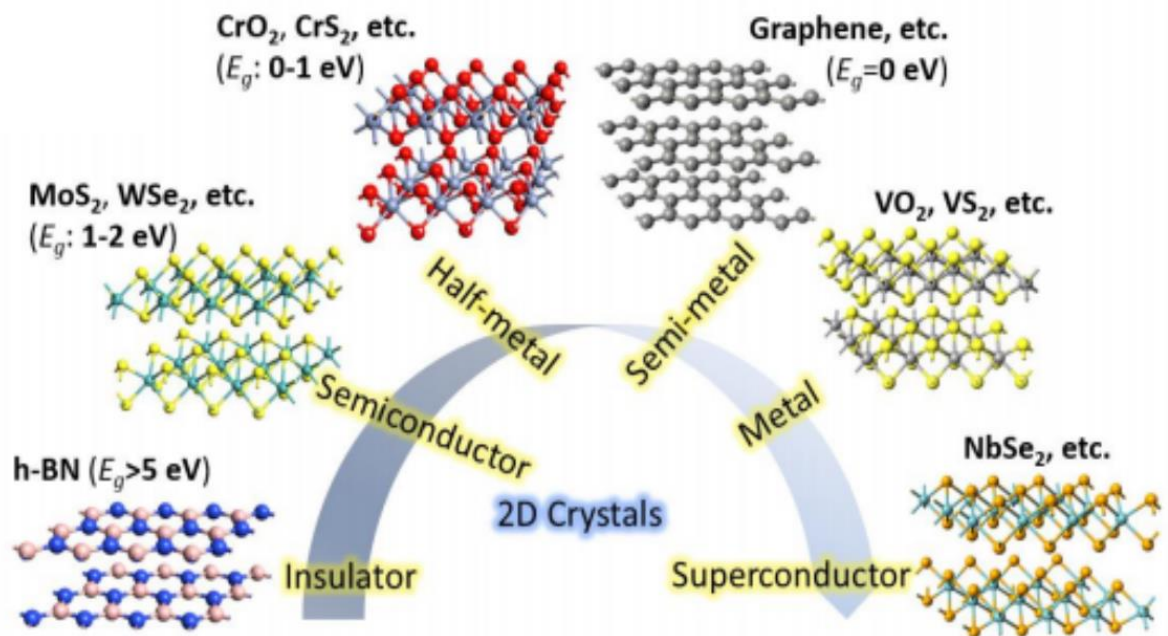


Figure 1.1 Various types of 2D materials from insulator to superconductor. E_g denotes the band gap from ref. [12]

The ground-breaking work of Novoselov et al[1], who were able to separate a single layer of graphene from graphite through micromechanical cleavage showed that these mono-layers indeed exist [1]. Scientists, then, have been looking for alternative methods to produce single layers of various 2D materials including chemical and liquid-phase



exfoliation of single layers from their bulk crystals [13, 14], and chemical vapour deposition (CVD) growth of 2D materials [15, 16]. There are different pro and cons in these methods. For example, the lateral size of the exfoliated 2D materials is typically of the order of micrometres by using mechanical cleavage [5, 17]. Chemically exfoliated 2D materials usually possess an irreversible chemical modification of their structure and properties [18]. Although CVD growth technique can produce macroscopic areas of 2D material films; it is still difficult to grow a continuously and uniform film because CVD growth needs a dedicated experimental setup and specific conditions for each 2D materials.[16].

Compared to other methods, the scotch tap based mechanical cleavage is the fastest and easiest way to obtain good structural quality atomically-thin layers of 2D nanomaterials, including Graphene, MoS₂, WSe₂ and NbSe₂ [1, 19-23]. This method allows us to have a direct investigation of the intrinsic properties of 2D materials.

Many techniques have been established to characterize these 2D materials, such as scanning electron microscopy (SEM) [24], transmission electron microscopy (TEM) [25], Raman spectroscopy and optical microscopy [21, 26]. Among these different techniques, Raman spectroscopy is a powerful and sensitive technique for the rapid identification and characterization of 2D materials [20, 27]. It is commonly used for the study on the structural changes of 2D materials [28].

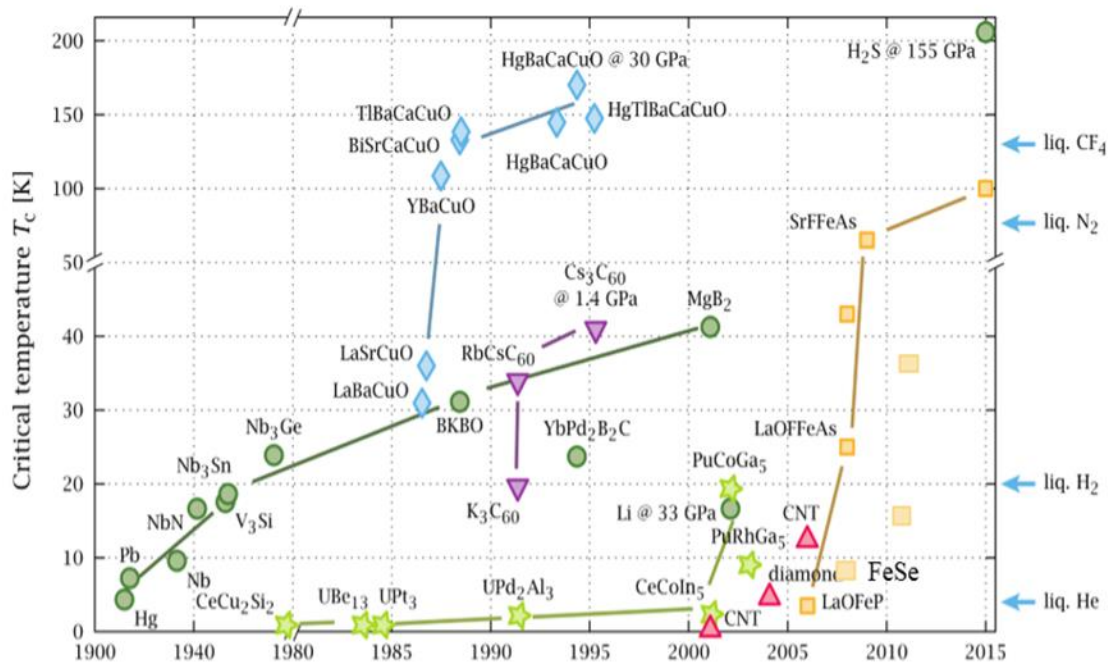


Figure 1.2: Timeline of Superconductor from Ref. [29]

As shown in Figure 1.2 shown, superconductor was first discovered in the early 1900, when the scientists cooled mercury to liquid helium temperature, 4K, and its resistance suddenly disappeared [30]. Afterwards, researches have put a lot of efforts on finding potential superconductor materials.

Since the discovery of $\text{LaO}_{1-x}\text{F}_x\text{FeAs}$ as a high-temperature superconductor in 2008 by Hosono group in Tokyo Institute of Technology [31], it has sparked a great interest in iron-based superconductivity. Soon after this discovery, another group has raised the superconducting transition temperature T_C up to 55K by replacing La with other rare-earth elements, which is now called the “1111” phase. [32].

For the Fe-based superconductor families, there are normally two different approaches in which superconductivity can be achieved. i.e. through charge doping and/or physical pressure [33]. For example, the T_C of undoped 1111-type LaOFeAs was



increased by inducing pressure [34]. These two approaches, however, decrease the critical temperature of 111-type LiFeAs [35].

1.2. Property of 2D materials

1.2.1. Molybdenum disulphide (MoS_2)

In a single layer of MoS_2 films, Mo (+4) and S (-2) atoms are arranged in a sandwich structure by covalent bonds in a sequence of S–Mo–S [36], whereas the sandwich layers are interacted by relatively weak van der Waals forces (Figure 1.3(a)). Generally, each layer has a thickness of ~ 0.65 nm. Monolayer MoS_2 with trigonal prismatic polytype is found to be semiconducting (referred to as 2H), while that with octahedral crystal symmetry configuration (referred to as 1T) is metallic (Figure 1.3 b) [37]. Very similarly to graphene, MoS_2 is mechanically flexible with a Young's modulus of 0.33 ± 0.07 TPa [38].

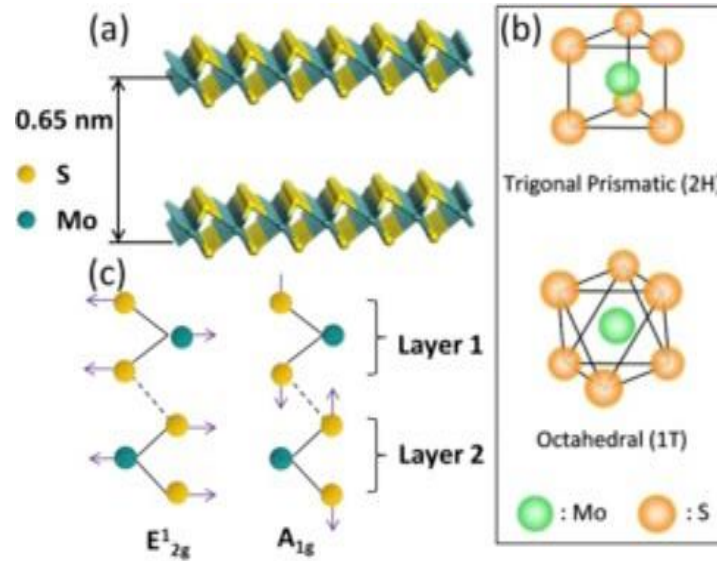


Figure 1.3 Crystal structure of MoS₂. (a) Chemical structure of two layers of MoS₂. (b) Two polytypes of single layer MoS₂: trigonal prismatic (1H) and octahedral (1T). (c) Schematic illustration of the two typical Raman active phonon modes (E_{2g}¹ and A_{1g}¹) from Ref.[39].

Raman spectra is a very direct and convenient characterization tool to illustrate the evolution of structural parameters in layered materials, especially when materials changing from 3D to 2D van der Waals bonded constructions in 2D materials [39, 40]. In early 2010, a systematically characterized study of single- and few-layer MoS₂ were studied by using Raman spectra [41]. Two Raman peaks E_{2g}¹ and A_{1g}¹ were investigated to reflect the crystal structure of MoS₂ [41]. These two Raman peaks are often used as indicators of in-plane and out-of-plane vibration modes of S atoms, respectively (Figure 1.3 (c)) [41]. Hong Li's group reported that the feature peak E_{2g}¹ exhibits a regularly blue-shifted while the other peak A_{1g}¹ shows an opposite red-shifted (shown in Figure 1.4 and Table 1) as the number of MoS₂ layer decreases [42]. From Table 1, it is noticed that that the frequency spacing is about 25 cm⁻¹ and 19 cm⁻¹ for bulk and monolayer MoS₂ respectively.

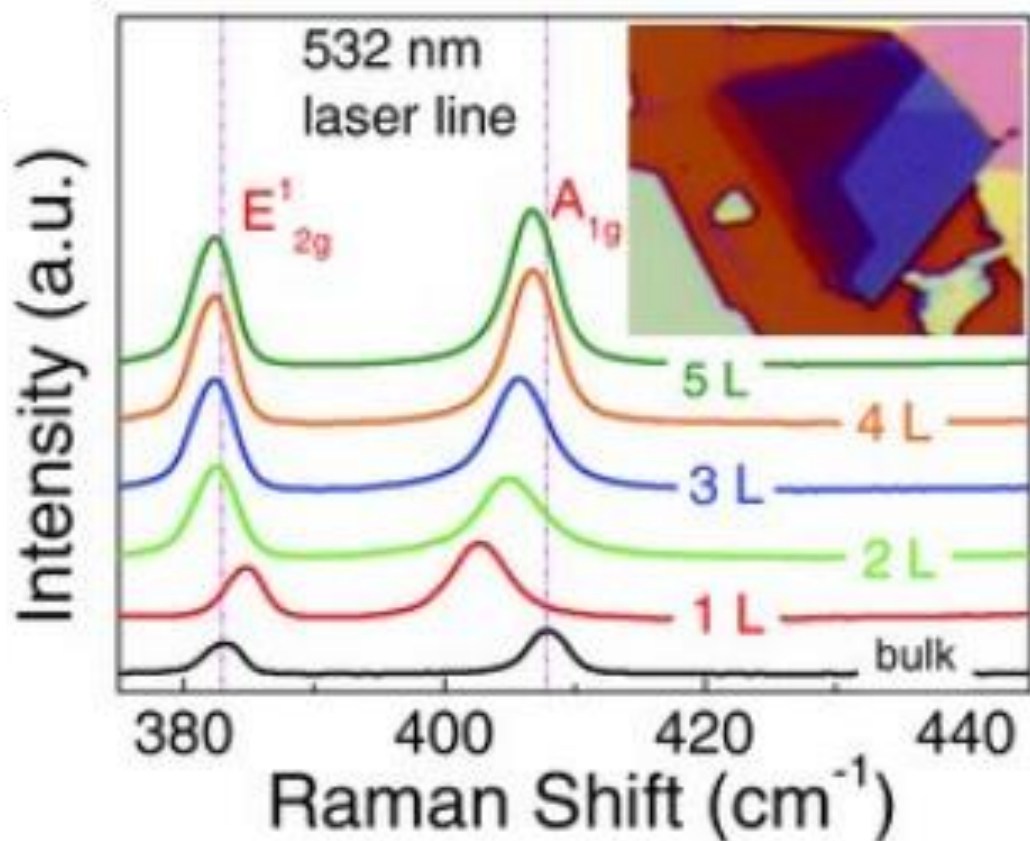


Figure 1.4 Raman characterizations of sample S2 using 532 nm line. The Raman spectra of different locations with various thicknesses on sample S2. Inset: optical image of sample S2. The left and right dashed lines indicate the positions of the and peaks in bulk MoS₂, respectively. The scale bars represent 2 μm. “1 L”, “2 L”, “3 L”, “4 L”, and “5 L” indicate monolayer, bilayer, trilayer, quadrilayer, and quinquelayer, respectively from ref. [42]



Layer	Raman Shift of E_{2g}^1 (cm^{-1})	Raman Shift of A_{1g} (cm^{-1})	Feature Peaks Separation (cm^{-1})
1L	384.7	402.8	18.1
2L	383.3	405.5	22.2
3L	383.2	406.5	23.3
4L	382.9	407.4	24.5
Bulk	383	408	25

Table 1 Summary of the E_{2g}^1 and A_{1g} peak frequencies measured by a 488nm laser. “1 L”, “2 L”, “3 L”, and “4 L” indicate monolayer, bilayer, trilayer, and quadrilayer, respectively. A single data represents the average value from three different samples from ref. [42].

Furthermore, photoluminescence (PL) spectra are found to be closely related to the number of layers in MoS_2 . As shown in Figure 1.5 two evident absorption peaks at 670 nm and 627 nm, identified as A1 and B1 excitons, are observed in the spectrum for 1L MoS_2 , while they both disappear in bulk MoS_2 [43]. Splendiani’s group assigned it as the two excitons to be associated with the energy split from valence band spin-orbital coupling [43].

In term of electrical performance, monolayer MoS_2 has a large direct bandgap of 1.8 eV, which is suitable for switching Nano-devices. The mobility of MoS_2 could be up to $200 \text{ cm}^2/\text{Vs}$ at room temperature with the current on/off ratio to be 1×10^8 [22]. Generally, MoS_2 is a n-type semiconductor [44], and it has a very outstanding performance in area of photocurrent generation and annihilation [45].

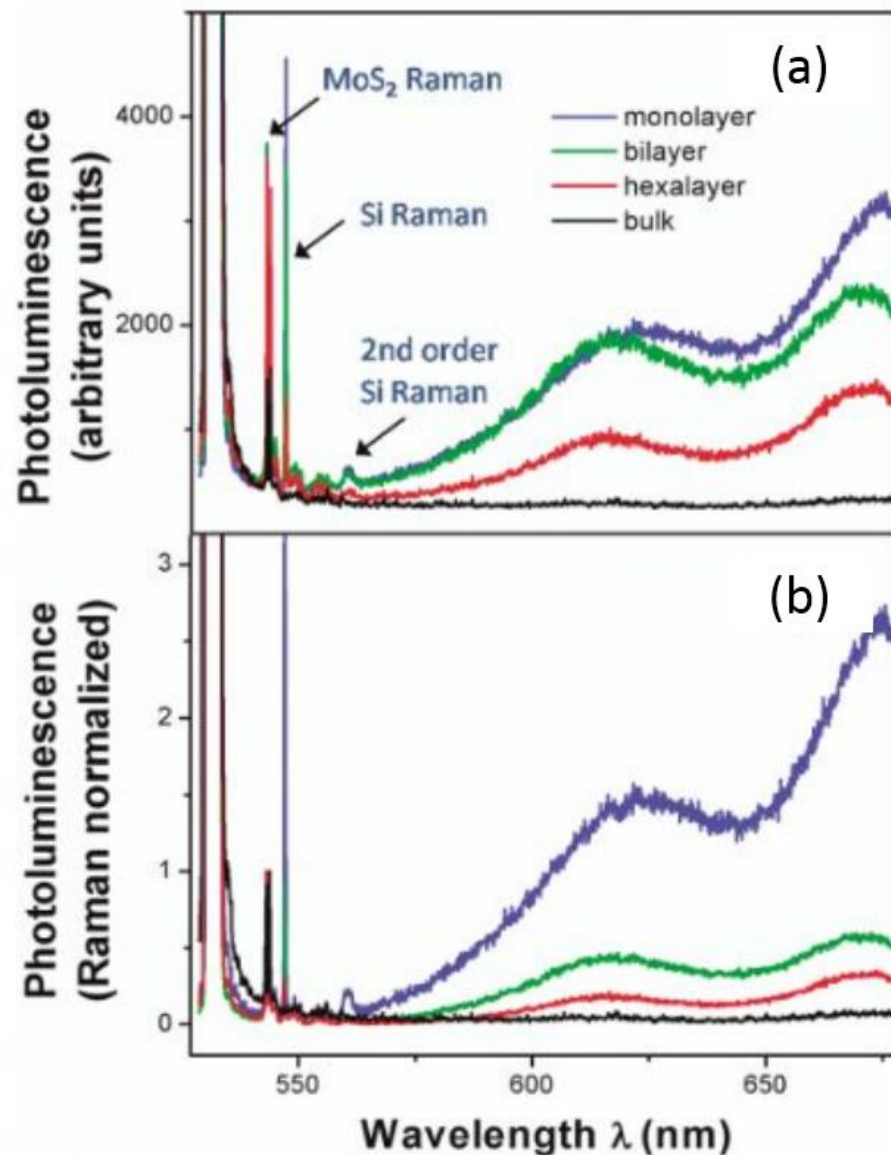


Figure 1.5 Layer dependence of photoluminescence efficiency in MoS₂. (a) Photoluminescence and Raman spectra of MoS₂ monolayer, bilayer, hexalayer, and bulk sample. Different Raman peaks can be assigned to the MoS₂ and silicon vibration modes. For MoS₂ thin layers, monolayer MoS₂ Raman signal is relatively weak because less material is being excited. However, photoluminescence is the strongest in monolayer MoS₂ in spite of reduced material. (b) Photoluminescence spectra normalized by Raman intensity for MoS₂ layers with different thickness, showing a dramatic increase of luminescence efficiency in MoS₂ monolayer from ref. [42, 43].

1.2.2. Iron Selenide (FeSe)

Since the report of superconductivity in PbO type FeSe at 8 K in 2008 [46], it has brought tremendous interest to other scientists. FeSe is composed of only FeSe layers with a tetragonal structure at room temperature as illustrated in Figure 1.6 (a) [47]. The crystal structure of FeSe possesses of a continuous stacking of FeSe layers, where a square-lattice layer of iron atoms is sandwiched between two twice-sparsely layers of bonding chalcogenide atoms within P4/nmm space group [47]. The crystal structure of FeSe is the simplest with a less toxicity than iron pnictides among Fe-based superconductors. Thus, these nature advantages of FeSe superconductor have attracted a lot of researchers using FeSe as the key material to elucidate the mechanism of Fe-based superconductivity. In addition, FeSe shows a structural phase transition at around 90K from tetragonal to orthorhombic phase, and becomes superconductor below $T_C \approx 8.5\text{K}$ [48].

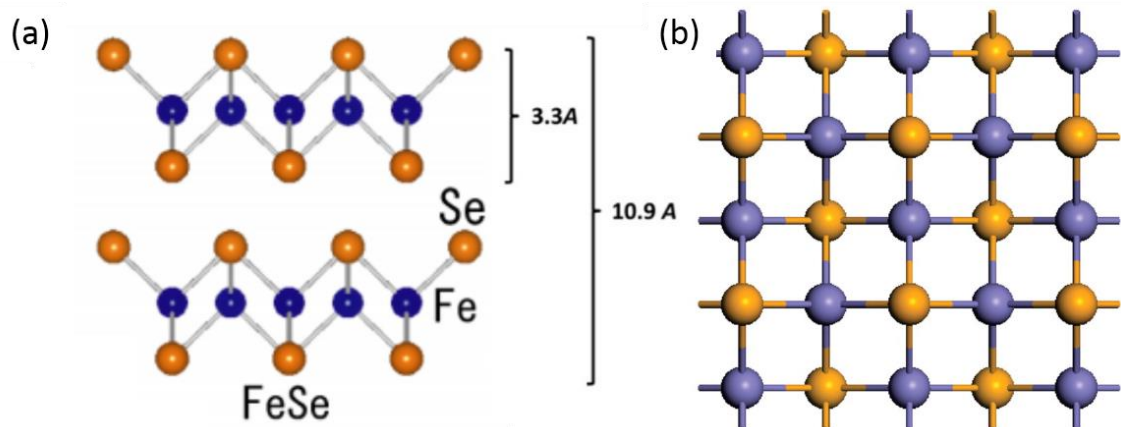


Figure 1.6 Crystal structure of FeSe from ref. [47].

1.2.3. Iron Telluride (FeTe)

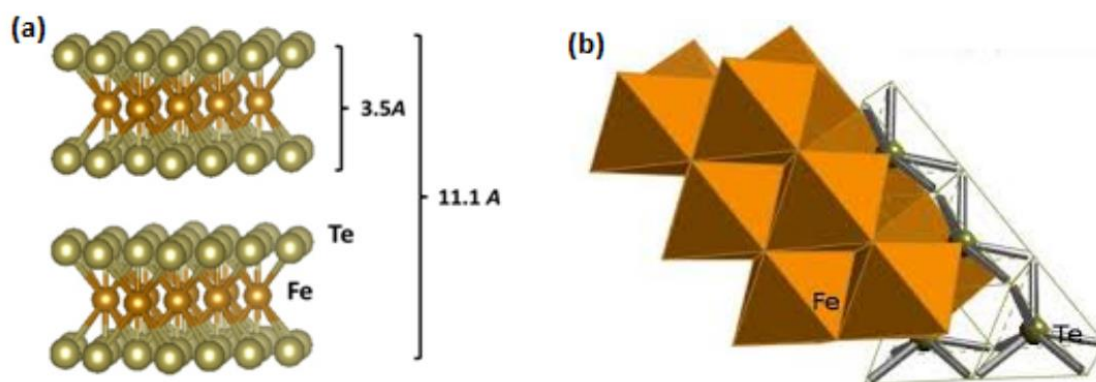


Figure 1.7 Characterizations of atomically thin FeTe samples. (a) Three-dimensional representation of the structure of FeTe. Single layers, 11.1 Å thick. (b) Tetragonal structure of FeTe from ref. [49, 50]

Iron Telluride (FeTe) is metallic layered transition metal chalcogenide, and composed of nontoxic element. Thus, it is very worthy for further investigation [51]. FeTe is simplest system because it is composed of a simple stacking of Fe-chalcogen layer without any interlayer elements as depicted in Figure 1.7(a). Each layer consists of Te-Fe-Te but the Te layer is containing twice as much atoms compared to chalcogenide layers (Figure 1.7(a)). Generally, layers are very weakly coupled by van der Waals forces to its neighbouring layers, so that single crystals can be cleaved easily. It has a tetragonal structure at room temperature (Figure 1.7 (b)) [52]. Tetragonal FeTe has a structure very analogous to superconducting FeSe [49]. However, FeTe does not show any superconductivity. A transition around 80 K shows an anomaly change of resistivity due to its structural transition [51].

1.2.4. Arsenic Trisulfide (As_2S_3)

Chalcogenide glasses such as As_2S_3 are interesting materials that have applications in many fields, including photonics and phase-change memories [53]. Arsenic trisulfide is the most studied chalcogenide glass and deserves applications in optical coatings and infrared optics due to its resistance to moisture or chemical, excellent IR transmission, and large glass-forming tendency [54]. As_2S_3 is a layer-like structure with 4.2 \AA between each layer as shown in Figure 1.8. It possesses a direct bandgap at around 2.2 eV and has a melting point around $300 \text{ }^\circ\text{C}$ [53, 55]. It belongs to one of the intrinsic p-type semiconductors in group V/VI that with photo-induced and phase-change properties. It, however, has a low hole mobility ($10^{-10} \text{ cm}^2/\text{Vs}$) [56].

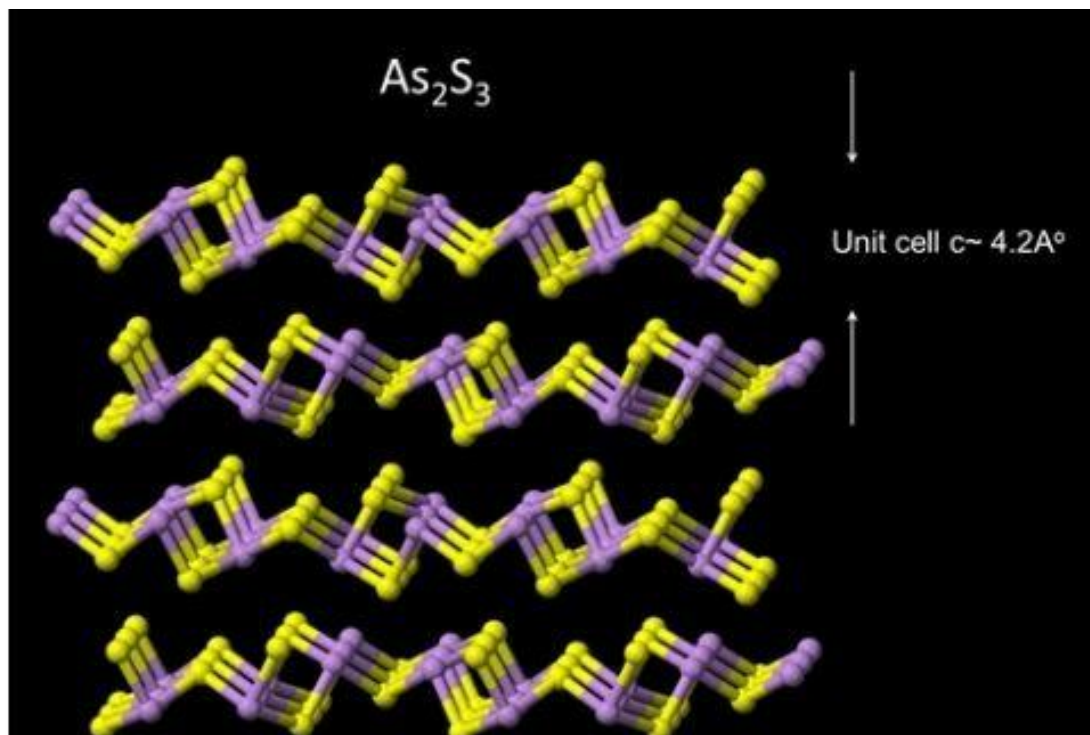


Figure 1.8 Structure of As_2S_3 from ref. [57]



1.3. Literature review

1.3.1. Strain Effect on MoS₂ by Raman Spectroscopy

Strain engineering is a powerful and widely used strategy for boosting the performance of optoelectronic, electronic and spintronic devices [58, 59]. The carrier mobility in semiconductors can be increased or the emission efficiency of light emitting devices by can be enhanced applying a strain through bending of films on elastic substrates or inducing a lattice mismatch between films and substrates [58, 60]. Generally speaking, the emerging 2D crystals such as MoS₂ are more favoured for strain engineering [61], as they have only one or a few atoms in thickness. Therefore, few layers or monolayer MoS₂, have attracted great interest because of their distinctive electronic and optical properties; especially their band gap has been highly sensitive to strain effect [5, 62].

In 2013, a group measured the Raman Spectra of compressively strained in tri-layer MoS₂ sheet on top of a piezoelectric actuator substrate [63]. For an applied strain of 0.2 %, the two feature peaks at 380 cm⁻¹ and 400 cm⁻¹ shifted by ~3 and ~ 2 cm⁻¹, respectively [63]. Another group from US studied the strain dependency of optical absorption and photoluminescence of atomically thin MoS₂ deposited on top of PMMA (ePlastics) [64]. They reported that under relatively small strains, a redshift of ~ 70meV/% strain was observed for the direct-gap exciton for both mono- and bi-layer MoS₂ [64].

1.3.2. P-N junction in 2D materials

The p-n junction is the basic building blocks in electronics since it has a vast range of applications such as rectifying diodes, light emitters, optical sensors and photovoltaic solar cells [65]. 2D materials have become the next key building blocks for p-n junction



which holding great promise for nanoelectronics. In this respect, heterojunctions of 2D materials are of great interest.

Among various 2D transition metal dichalcogenides (TMDC) semiconductor, few layer-thin MoS₂ is a well-known n-type semiconductor, since it displays a high on/off current ratio, excellent carrier mobility and a good sub-threshold swing in field-effect transistor (FET) [17, 36, 66-74]. Relying on the van der Waals interactions, atomically sharp 2D heterostructures can be achieved without the problems caused by lattice mismatches between materials [72]. Many TMDC junction systems have been fabricated in order to study the properties of 2D based P-N diodes. For example, n-MoS₂/p-Si bulk [70, 75], n-MoS₂/p-WSe₂ [66, 70, 76, 77] and n-MoS₂/p-Black phosphorous junctions [72] have shown distinctive properties.

In 2014, Deng's group reported an electrically gate tuneable black phosphorus-monolayer MoS₂ van der Waals heterojunction p-n diode [72]. They showed that 2D p-n diodes exhibit strong gate-tuneable current-rectifying I-V characteristics. As a photodetector, the p-n diode shows a photo detection responsivity which is nearly 100 times higher than the reported black phosphorus phototransistor which is very suitable for broad-band and sensitive photo detection [72].

A research team led by Jong Tae reported a p-n diode made of n-MoS₂/p-WSe₂ [36]. This p-n diode shows a high photo responsivity at zero volt without any electric power, and it appears comparable to those of commercially-optimized Si p-n diode [36]. They have maximized the photovoltaic energy benefits with optimized TMDC thickness [36].



1.3.3. Superconductivity in Iron-Based 2D materials

Superconductors have many applications. One of the common applications for our future is to transport electricity without loss of energy. Other promising future applications include high performance transformers, power storage devices and magnetic levitation devices etc. Furthermore, magnetic resonance imaging (MRI) using superconductor has been widely employed in medical facilities.

Early pioneering studies aimed at probing superconductivity in layered materials can be date back to the 1970s [78, 79], but only over the last few years the experimental control necessary to unambiguously identify the thickness of atomically thin layers has been developed. Only until recently researchers have paid much intention into 2D superconductors. For example, a group reported that transition temperature (T_c) of 2D superconductor NbSe₂ decreased when the number of layer decreased[80]. It shows a good indication that properties of 2D superconductor are worth being studied. A limited number of research has been conducted on other 2D superconductors in particularly layered Iron-based chalcogenides.

Iron-based superconductors showed a very promising result in the past few years (Figure 1.2). Superconductivity of the layered Iron-based chalcogenides was revealed in FeSe with $T_c \sim 8\text{K}$ [46]. T_c of substituted compounds FeSe_xTe_{1-x} reached up to $\sim 14\text{K}$ at $x=0.4$ [50]. Under hydrostatic pressure, T_c of Fe_{1+y}Se was enhanced to $\sim 37\text{K}$ around 7-9 GPa and T_c even increased up to 100K in a single-layered FeSe film grown on SrTiO₃



substrate. Together with the observation of its unique electronic structure and nodeless superconducting gap, these studies have generated much interest among scientists[81-83].

Until now, it is still a question to debate whether superconductivity can be observed in FeTe [84]. Several recent studies have suggested that the FeTe layer has the potential to produce superconductivity if (i) Te is substituted by small elements like Se or (ii) under interfacial stress, and more specifically tensile stress. These methods can turn FeTe into tetragonal FeTe compound by inducing chemical pressure [51, 85].

1.4. Objective of research

The unique and extraordinary properties of 2D materials have aroused the attention of many scientists since the discovery of graphene. Some scientists have paid much attention and afford to discover high transition temperature superconductors in 2D materials [86], study the electrical properties of monolayer 2D materials and fabricate flexible 2D electronic devices [38]. In this thesis, we will focus on the investigation of optical and electrical properties of 2D materials. A gap in our understanding of the relationship between Iron-based 2D materials and its Raman spectra needs to be filled. For example, if a relationship similar to the identification of individual and few layers WS₂ by using Raman spectroscopy can be established for those Iron-based 2D materials [11], then Raman spectroscopy can be used as an useful and direct tool to identify the thickness of Iron-based 2D materials instead of using atomic force microscopy.

Furthermore, the effects of strain on CVD monolayer MoS₂ have been extensively studied for recent years [87]. These studies have demonstrated great advantages that can be very useful for the development of optoelectronic devices. However, limited research has been conducted on the strain effect on exfoliated MoS₂ along different MoS₂



directions. Here, we have demonstrated a modified bending technique to apply precise uniaxial tensile strain along different directions of MoS₂ together with these measurements of Raman spectra, on the basis of our measurements, we hope that the Armchair and Zigzag directions of the exfoliated MoS₂ can be determined by monitoring the variation of Raman Shift in different strained directions.

Most of the 2D semiconductors are intrinsic n-type semiconductors. Due to the lack of intrinsic p-type semiconductor, few investigations have been done to study the properties of p-n junction of 2D semiconductor and also the effect of electrode preparation on these 2D materials. In this thesis, we have tried to study the electrical properties of p-As₂S₃ / n-MoS₂ and also to investigate the effect of electrode preparation on low melting point material like As₂S₃ by using Raman spectroscopy.

Very few 2D superconductors exist in nature, iron-based 2D materials like FeSe are categorized in this group. Hardly any study has been conducted on these iron-based 2D materials. This thesis attempts to investigate the superconductivity behavior of exfoliated FeTe and FeSe.

1.5. Outline of thesis

The sequence of the thesis arrangement is as the following described:

In chapter 1, a brief introduction on 2D materials is presented and properties of MoS₂, FeSe, FeTe and As₂S₃ are listed. Furthermore, literature review of strain effect on MoS₂ by Raman spectroscopy, p-n junction in 2D materials and superconductivity in iron-based 2d materials are introduced. The objectives and outline of this thesis are also contained in this chapter.



Chapter 2 introduces the experimental techniques and various characterization methods. Basic principle of photolithograph, magnetron sputtering, e-beam evaporation, mechanical exfoliation and dry transfer method are summarized. This chapter also introduces the measurement techniques such as AFM, Raman spectroscopy measurement, two-point and four-point measurement.

After that, chapter 3 describes the optical characterization of MoS₂ and FeTe. The fabrication of the modified bending technique for MoS₂ and also the respond of its Raman peaks to the different strained directions are discussed. The next section talks about the thickness dependency of FeTe Raman spectra.

Chapter 4 mainly focuses on the electrical properties of 2D materials. At first, effect of electrode preparation on As₂S₃ is discussed. Then the result of I-V characteristic of p-n junction is discussed. The next section presents the superconductivity behavior in the iron-based 2D materials including FeTe and FeSe.

Conclusion and future work are presented in chapter 5. In this chapter, the results of this thesis are summarized and concluded. Meanwhile, future work on different 2D materials is suggested in this chapter.



2. Methodology

In this chapter, principle of fabrication methods and characterization techniques used in this project are introduced. This chapter is divided into two sections: (i) substrate patterning and sample fabrication methods and (ii) the equipment used for characterization of structural morphology and optical properties measurements of the 2D materials.

2.1. Substrate patterning and Sample Fabrication Methods

2.1.1. Photolithography

Photolithography, also known as UV lithography or optical lithography, is a process typically used in microfabrication to do patterning on a thin film or a bulk substrate. This technique is commonly used to create extremely small patterns (~1 μ m in size). It involves light exposure through a photomask to a light-sensitive “photoresist” chemical, then the photoresist is developed to form three-dimensional relief image on the substrate. In an ideal case, photoresist image has the exact geometric pattern of the desired pattern on the plane of the substrate. Thus, the final resist pattern is binary i.e.: parts of the substrate are completely uncovered with resist while other parts are covered. To achieve a high quality pattern transfer, this binary pattern is needed since the parts of the substrate covered with resist will be protected from etching, deposition, or other pattern transfer mechanisms.

The general sequence of processing steps for a typical photolithography process is divided into 7 parts: (i) substrate preparation, (ii)photoresist spin-coat, (iii)pre-bake, (iv) exposure, (v)post-exposure bake, (vi)development, and (vii)post-bake. At the end,

users can either choose to etch the substrate or deposit desired materials on top of it.

Figure 2.1 is the UV contact aligner (OAI 800) with 450W UV light.

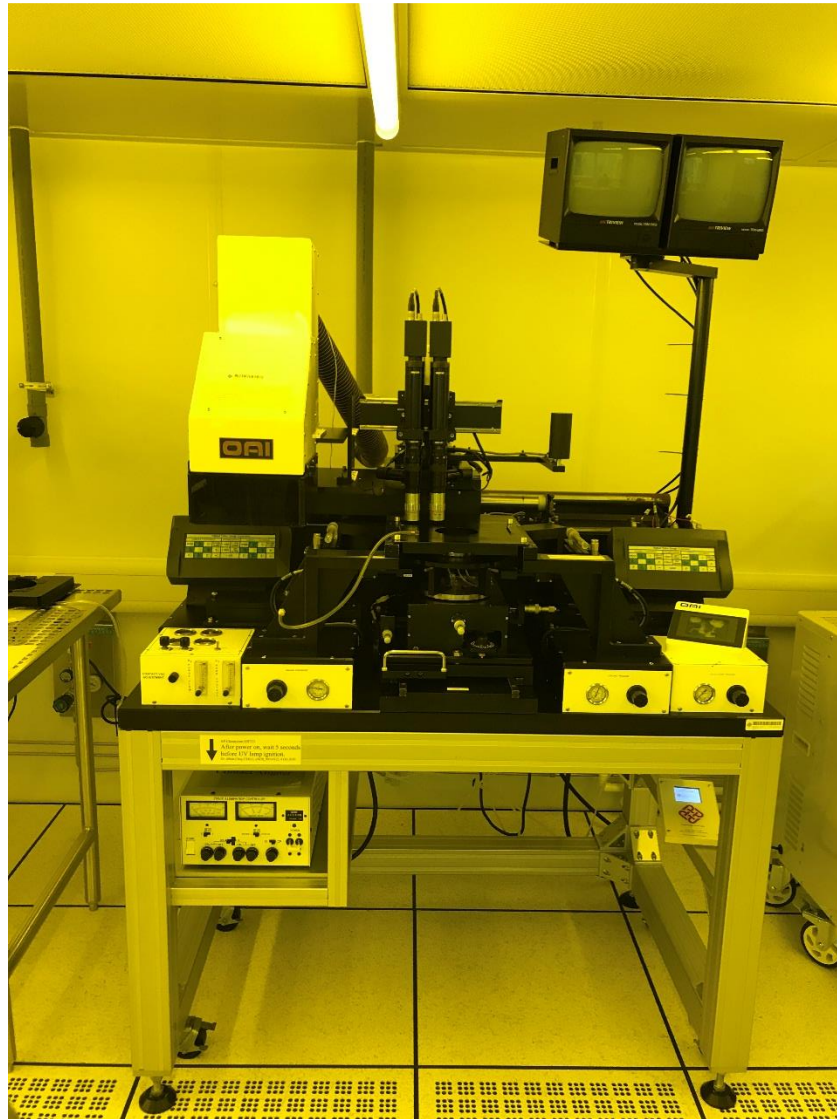


Figure 2.1 UV contact aligner

2.1.2. Magnetron Sputtering

Sputtering is a common physical vapor deposition technique that allows different “targets” (oxides, metals or semiconductors) to be deposited on top of substrates[88]. This technique is mainly dependent on the establishment of direct-current (DC) discharge present between the surface of target and the substrate[89]. During the deposition process,



a plasma is created and positively charged ions from the plasma are accelerated by an electrical field superimposed on the negatively charged “target”. The positive ions are accelerated by potentials, and strike the negative electrode with sufficient force to dislodge and eject atoms from the target with a very high kinetic energy[90]. As a result, these atoms might penetrate through the surface of substrate with a depth of about centimetres and will be ejected in a typical line-of-sight cosine distribution from the face of the target. The ejected plasma will condense on surfaces that are placed in proximity to the magnetron sputtering cathode. The experiment is conducted under the level of pressures at about ten millitorr to ensure the efficiency of film production becomes reliable[91, 92]. The schematic diagram and the experiment setup of the D.C. magnetron sputtering system used in our project is shown in Figure 2.2 (a) and (b) respectively.

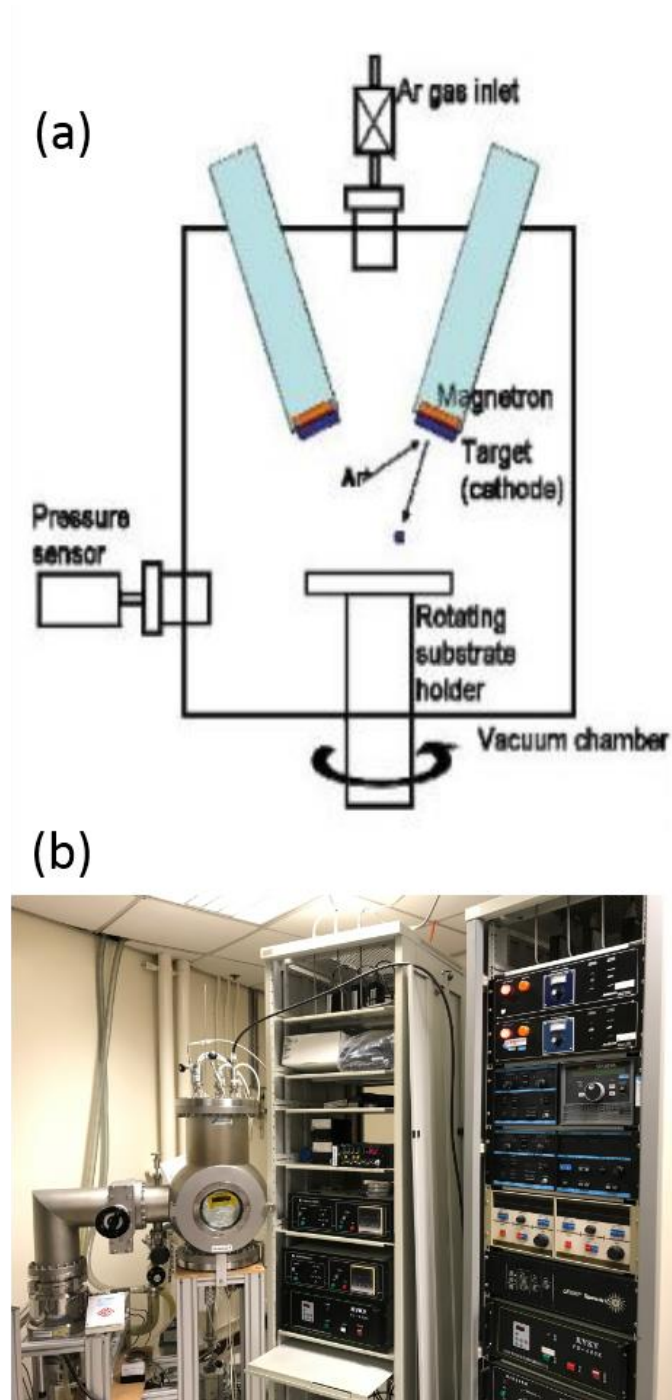


Figure 2.2 (a)Schematic diagram of the D.C magnetron sputtering system (b) The experimental setup of the D.C. magnetron sputtering system used in this work.



2.1.3. Electron beam Evaporation

Electron Beam Evaporation (E-beam) is another commonly used physical vapour deposition method. It is a high vacuum deposition technique that is commonly used for thin film fabrication or deposition of metal coating on the surface of various materials. To generate an electron beam, a current is sent through a filament which is located in an area outside the deposition zone to avoid any contamination. The filament is heated until the thermionic emission of electrons occurs and magnets are used to focus the electrons to form a beam which is directed toward a crucible. The crucible is then heated by the beam so that the material inside the crucible is evaporated and converted into a gaseous state for deposition. The material vapour vaporizes toward the sample and coat on top of it. Figure 2.3 and Figure 2.4 are the schematic diagram of E-beam evaporation and the photo of the E-beam evaporation equipment used in our work.

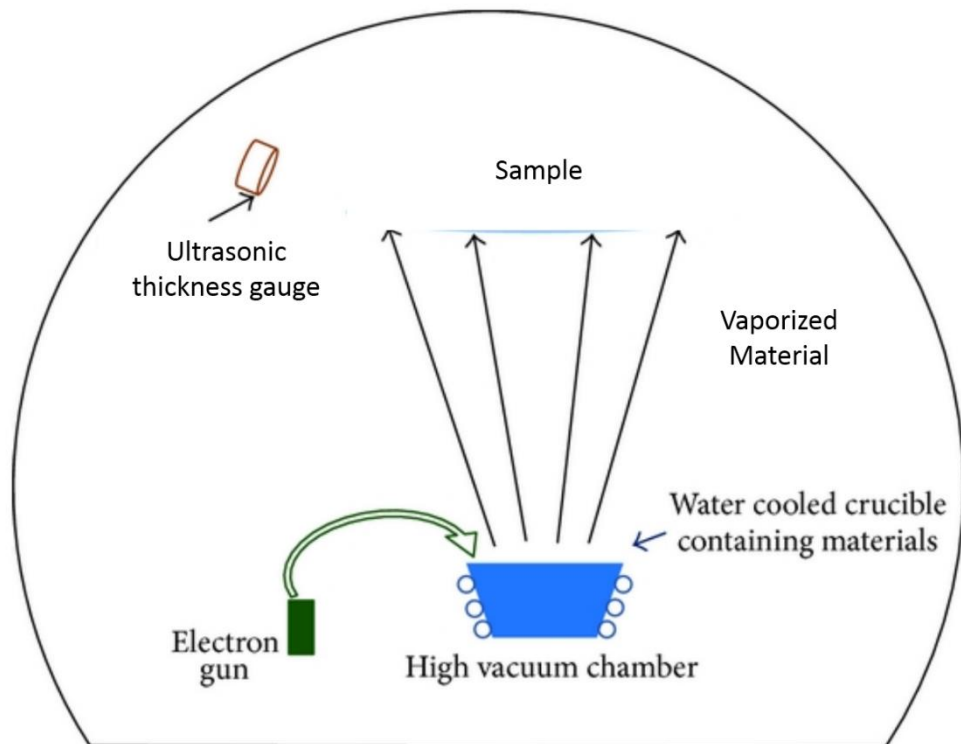


Figure 2.3 Schematic Diagram of Electron Beam Evaporation from ref. [93]



Figure 2.4 Electron Beam Evaporation



2.1.4. Mechanical Exfoliation

2D materials of van der Waals layered structure can be prepared by mechanical exfoliation. For example, graphene is prepared by exfoliating graphite. The concept of this mechanical exfoliation is that monolayer 2D materials can be peeled from their bulk single crystal layer by layer. Van der Waals attraction force between the layers, is the main resistance needed to be overcome in order to achieve a monolayer 2D material. The attraction force can easily be overcome by mechanical forces. In general, there are two mechanical forces. The first one is the normal attraction force between layers and this is the force that needed to be overcome when peeling two layers apart. A typical example is micromechanical cleavage by Scotch tape[1, 19]. Another one is the lateral force that comes from the self-lubricating ability in the lateral direction of those 2D materials[94].

2.1.5. Dry Transfer

The first all-dry technique for transferring 2D materials, developed by a team led by Herre van der Zant and Gary Steele in Netherlands, has brought huge impact to research in 2D materials [95]. In their studies, a thin layer of a commercially available transparent viscoelastic material called “Gelfilm” was used, and the thinnest flake was selected by using an optical microscope which was fixed onto a XYZ sample stage just shown in Figure 2.5 (a). As the stamp was transparent, the sample could be seen through under the optical microscope and the flake could be aligned with wherever desired substrate. To transfer the flake, the stamp was needed to be pressed against the sample surface and peeled off slowly [95]. As shown in Figure 2.5 (b), tri-layer graphene was then transferred on top of the boron nitride without any bubbles or wrinkles.

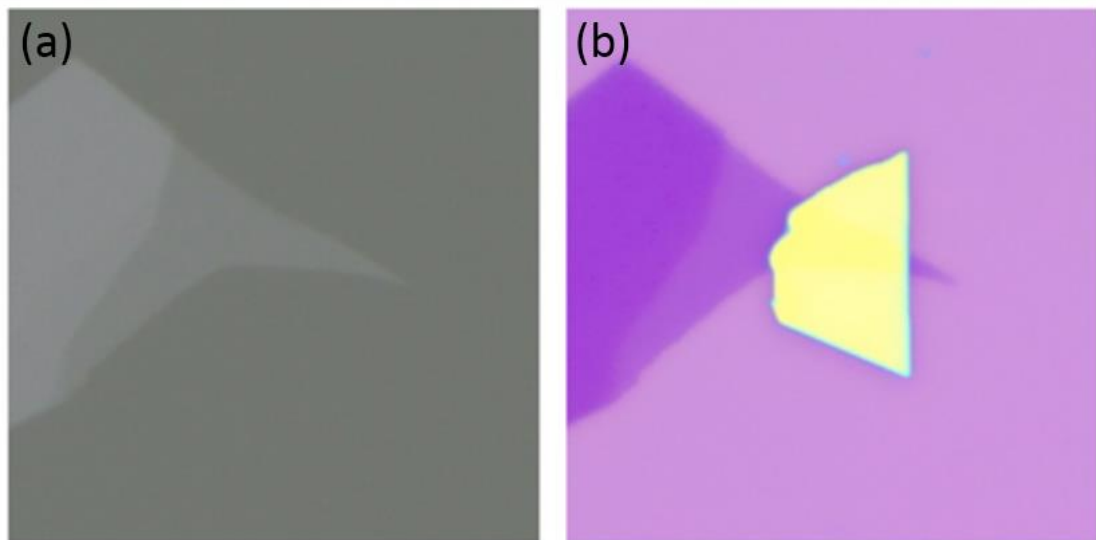


Figure 2.5 (a) SEM image of tri-layer graphene on the surface of the viscoelastic stamp (b) SEM image of tri-layer graphene transferred onto hexagonal boron nitride from ref. [95]

The working principle of this method is viscoelasticity. The stamps are made from a silicone rubber which is a viscoelastic material [95]. The stamp behaves like an elastic solid over small amount of time onto the surface and with longer timescales it can flow all over the surface until it becomes intimately joint to it. With this behavior, the flakes can be adhered to the stamps without applying any glues. To detach the flakes from the stamp surface, this can be achieved by peeling the stamp off slowly, the flake can stick to the desired substrate. Figure 2.6 is the experimental setup for doing dry transfer which consists of XYZ stage together with optical microcope.

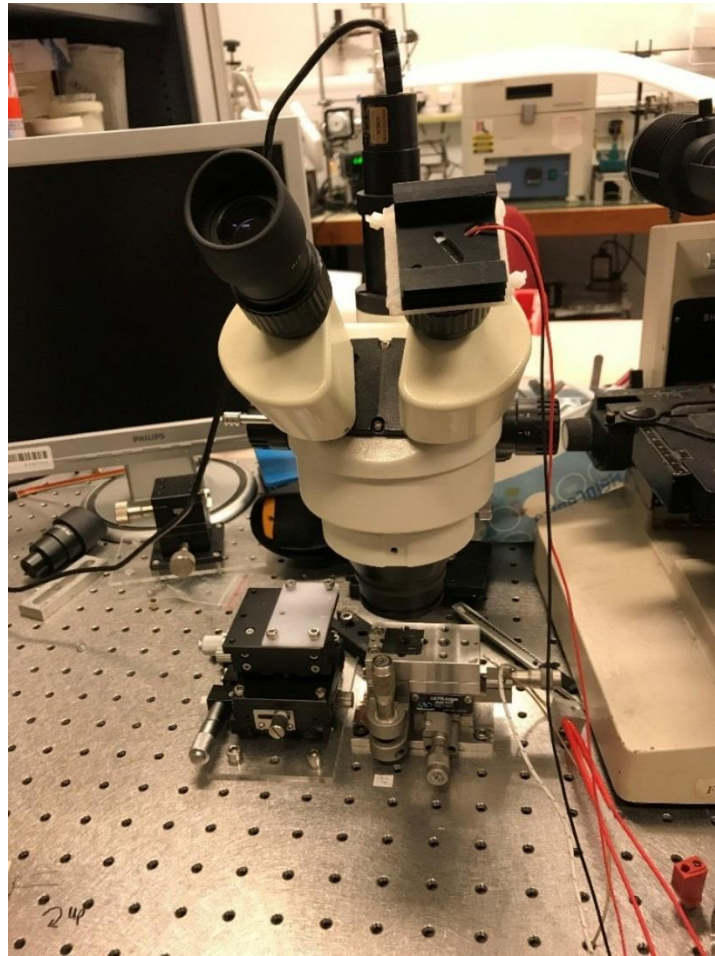


Figure 2.6 XYZ stage together with optical microscope for dry transfer

2.2. Characterization techniques

2.2.1. Atomic force microscopy (AFM)

Atomic Force Microscopy (AFM) is a tool that can provide nanoscale 3D image of the material surface. It is an important tool to be used for analysing the surface topology of materials. The working principle is shown in Figure 2.7 (a). AFM consists of a cantilever with a sharp tip at its end which is used to scan the specimen surface. When the tip is brought within the interatomic separation between the sample and tip, force between the tip and the sample lead to a deflection of the cantilever. Therefore, by measuring the deflection of the cantilever, the topographic features of the surface can be

mapped out. The deflection of the cantilever is usually monitored by using a laser and a detector as shown in Figure 2.7 (b). A laser beam illuminating on the backside of the tip is reflected from the cantilever, and the signal is detected. Then the surface morphology and three-dimensional images can be produced with the aid of software (NanoScope Analysis 1.5)

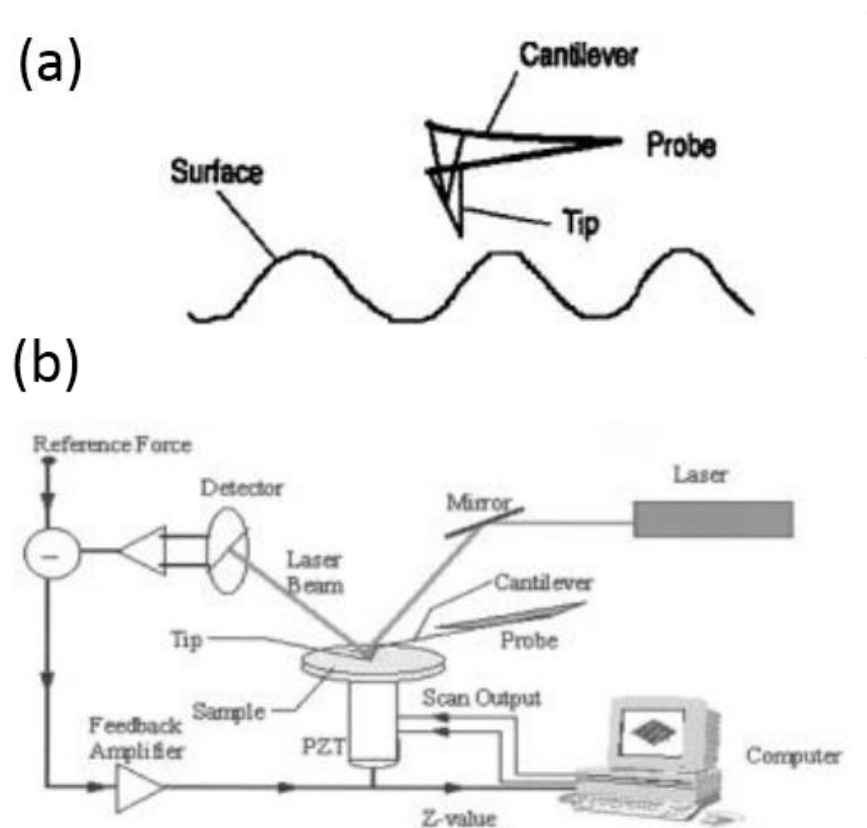


Figure 2.7 (a) Principle of AFM (b) schematic of AFM from ref. [96]

AFM can be operated in three different modes, namely, contact mode, tapping mode and non-contact mode. Among them, tapping mode is the most common by used as the tip does not contact with the sample surface directly, thus it is non-destructive to the samples. This mode, therefore, has many advantages, including overcome problems associated with friction, adhesion and viscosity. In this thesis, the type of the AFM used was Nanoscope 8 (Digital Instruments Ltd. Co.) which is shown in Figure 2.8.



Figure 2.8 Atomic force microscopy

2.2.2. Raman spectroscopy

Raman spectroscopy is a convenient and non-destructive characterization technique for chemical bonding identification, structural characterization, stress analysis and vibration mode detection by irradiating the monochromatic light on specimens [97]. The shift in wavelength (Raman shift) of the scattering photon provides the chemical and structural information. When the light is incident onto the specimen, the light will be scattered with excitations of bond vibration within between molecules and scattered photons will be different depending upon the vibrational state of the materials, and these photons will be collected by Raman spectroscopy. A simplified energy diagram is illustrated in Figure 2.9.

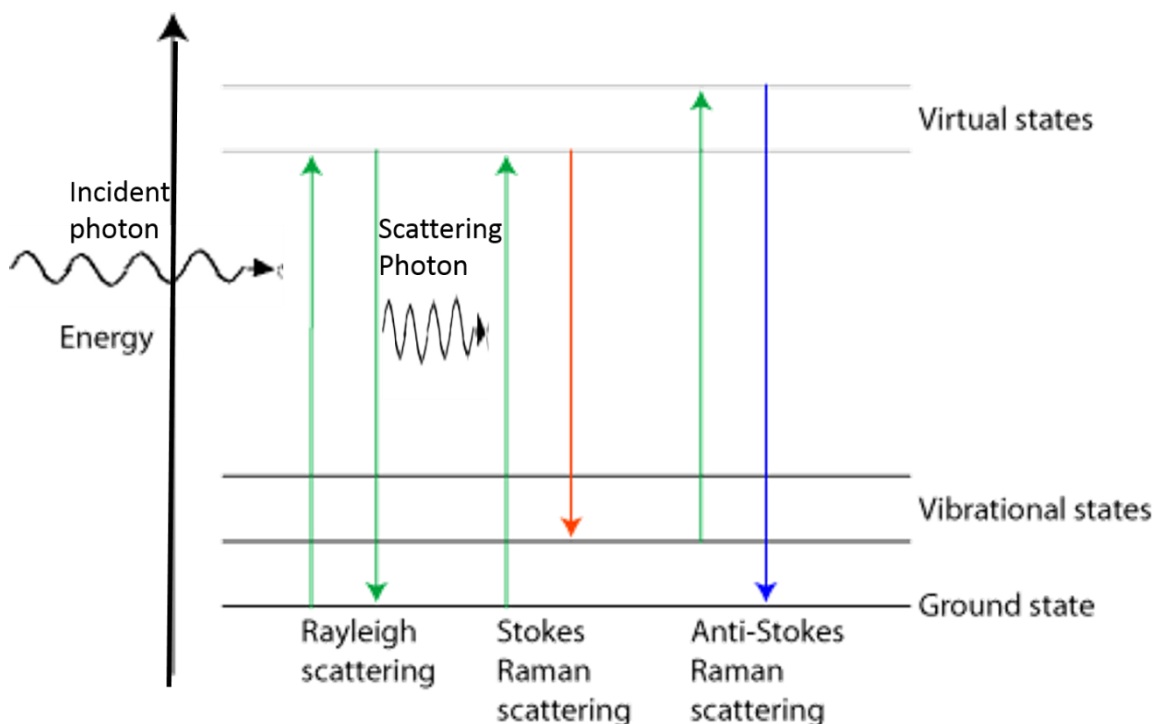


Figure 2.9 Schematic diagram of Raman scattering from ref. [98]

Figure 2.9 shows three conditions on excitation of molecules to upper vibrational levels. The phenomenon of inelastic light scattering is known as Raman radiation [99]. Firstly, Rayleigh scattering is a photon interacts with a molecule and raising the molecule to a “virtual” energy state soon then the molecule drops back to its ground state by releasing a photon. Since the molecule is dropping back to the same state, the energy in the scattered photon must be the same as the energy from the initial photon. Then, no information regarding the vibrational energy levels of the sample can be obtained, and this is called the Rayleigh scattering. If the molecule is promoted from a ground to a virtual state and then drops back to a vibrational state with higher energy, then the scattered photon has less energy than the incident photon with a longer wavelength, and this is called Stokes scattering. Anti-Stokes scattering is the reverse of Stokes scattering which the molecule is in a vibrational state to begin with and after scattering the molecules

is in its ground state, then the scattered photon has more energy with a shorter wavelength [99].

Raman spectroscopy is a technique to measure the shift between the incident and scattered light. The Raman shift is shown in the equation below.

$$RamanShift = \frac{1}{\lambda_{incident}} - \frac{1}{\lambda_{Raman\ Scattering}}$$

Raman shift can be used to identify the particular energy of vibrational bonds in the samples, which is representing to the corresponding bonding. Thus, the bond that composes the samples can be identified [99].

Horiba HR800 Raman microscope shown in Figure 2.10 system was used to measure the Raman shift of the 2D materials. This spectrometer has a spectral resolution $< 0.5\text{ cm}^{-1}$, which embedded with a 488 nm Ar^+ laser as incident source for the excitation of specimens. The emitted light from the sample is collected by a typical microscope via the 100 \times objective lens with a numerical aperture of 0.9 at room temperature. The spot size of $\sim 1\text{ }\mu\text{m}$ with a laser power of 180 mW was used.



Figure 2.10 Raman spectroscopy

2.2.3. Two-point & Four-point measurement

Ohm's law relates voltage V across a circuit component, current I through a circuit

component, and resistance R of that component, i.e. $R = \frac{V}{I}$ [100].

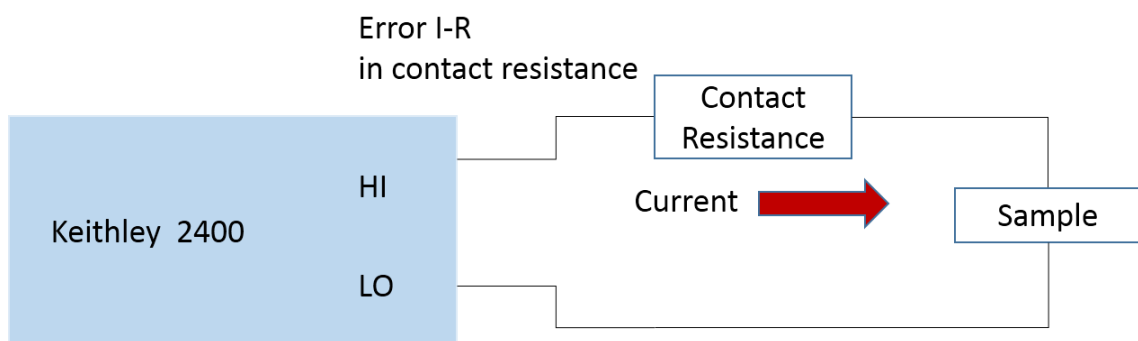


Figure 2.11 Two-wire resistance measurement configuration



Two-terminal Keithley 2400 source current test through the contact resistance and sample, terminating at the HI-LO inputs of the Keithley 2400 as shown in Figure 2.11. Keithley 2400 can be used as a source-measure unit, applying voltage to a device and measuring the current through it. With the help of LabVIEW program, an I-V characterize curve can be generated using Keithley 2400 as shown in Figure 2.12 (a). This two-wire ohms' system works fine for most resistance measurement applications. For measuring a small resistance (below 100 Ω), the I-R drop in the contact resistance can cause inaccuracies that become apparent in low resistance sample measurements[101]. Figure 2.12 (b) presents the experimental setup of Two-point IV characterize curve measurement.

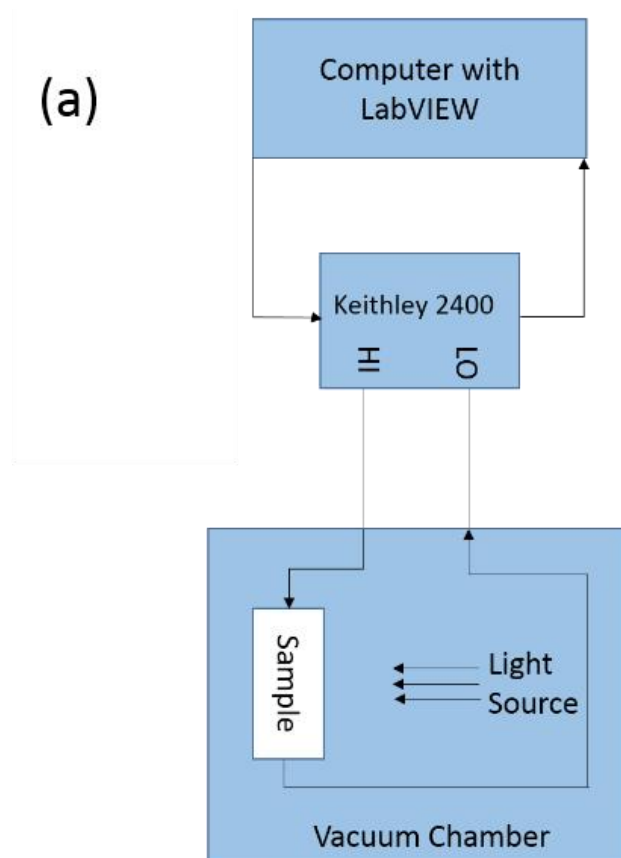


Figure 2.12 (a) Two-point IV characterize curve measurement configuration (b) The experimental setup of Two-point IV characterize curve measurement

Four-point measurement, also known as Kelvin measurement, is the way to bypass the voltage drops across contact resistance by bringing two high impedance voltage sense leads out to the resistance of our samples[102, 103], as shown in Figure 2.13. There is very little current in the sense circuit because of the high input impedance, so there is effectively no I-R drop in the contact resistance, and the voltage seen by the sense terminals is the same as the voltage developed across our samples[104, 105].

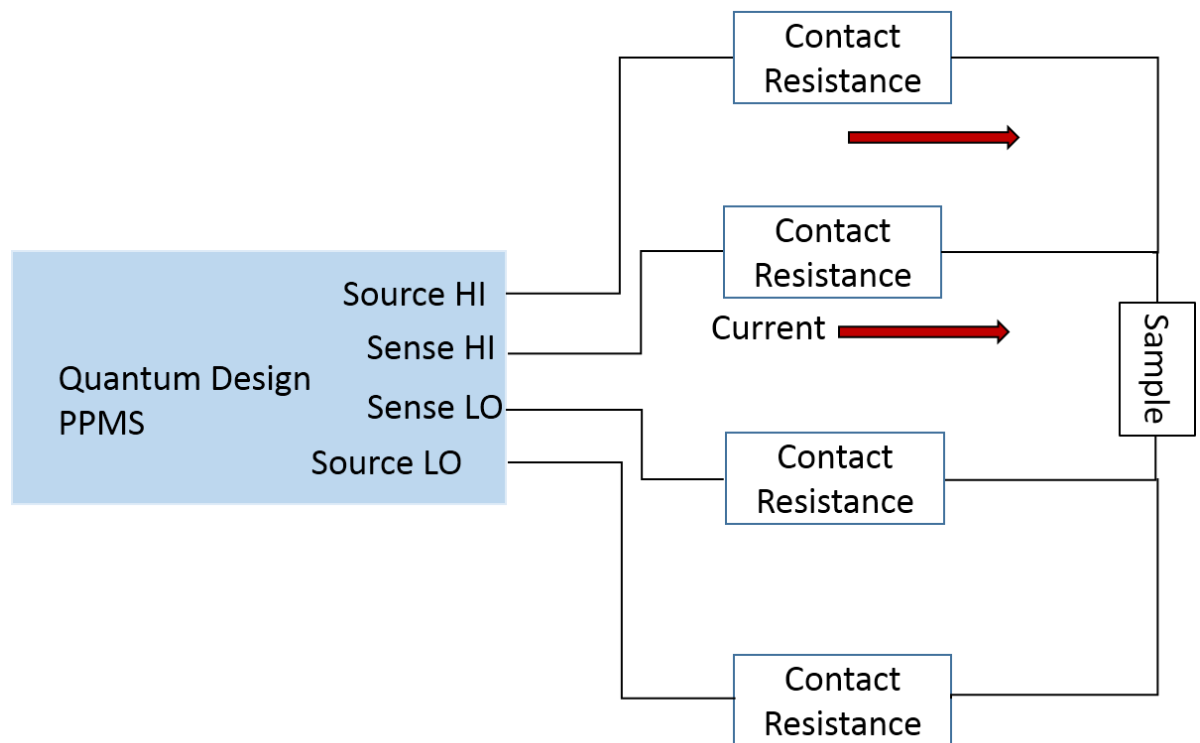


Figure 2.13 Four-point resistance measurement configuration

In my work, Quantum Design Physical Properties Measurement System (PPMS) was used to measure the resistance as well as the superconductivity behaviour in low temperature as shown in Figure 2.14. It has a sealed sample chamber with 2.6 cm diameter sample access with Continuous Low-Temperature Control that maintains temperature

below 4.2 K and offers smooth temperature transitions when warming and cooling through 4.2 K.



Figure 2.14 Physical Property Measurement System

3. Optical properties of 2-Dimensional Materials

This chapter presents an overview about the optical properties of MoS₂ and FeTe measured by Raman spectroscopy. It is divided into three sections: (i) preparation of MoS₂ and FeTe, (ii) Raman spectra in different strained directions of MoS₂ and (iii) Raman spectra for different thickness of FeTe. A modified bending technique for applying strain in different uniaxial directions for the sample is also introduced. The Raman shift rate of different thickness of MoS₂ being strained in different uniaxial directions is discussed. At the end, the relationship of different thicknesses of FeTe with respect to their thicknesses is discussed.

3.1. Preparation of MoS₂ and FeTe

3.1.1. MoS₂

Polyethylene terephthalate (PET), a transparent and conventional plastic, was used as the substrate for this experiment. Firstly, the PET was cut into an octadecagon shape with 24 mm diameter as shown in Figure 3.1. Schematic diagram of PET with octadecagon shape is shown in Figure 3.2. Octadecagon PET was then coated with SU-8 photoresist (≈ 400 nm) with a speed of 4000 rpm for 40s to enhance the visibility of MoS₂ and reduce the surface roughness of the PET which also serves to increase the adhesion of MoS₂ on

top of PET [106, 107]. The PET with a layer of SU-8 was then baked with 110°C for 10 minutes to evaporate the excess solvent of SU-8. The mechanically exfoliated MoS₂ was deposited at the centre of the PET substrate. As the size of the MoS₂ was very small compared to the thickness of PET, therefore the induced strain to the flakes can be assumed to be the same as the applied strain to the PET substrate [108]. At the end, a thin layer of Poly (methyl methacrylate) (PMMA) with thickness around 100 nm was immediately covered on top of the deposited MoS₂ using a spin-coater operated at a speed of 4000 rpm for 30s. The PMMA layer was used to prevent the slippage and protect the MoS₂ from degradation in ambient. The sample was then baked 110°C for 1 minute to harder the PMMA layer. Figure 3.3 shows the detailed fabrication process of MoS₂ encapsulated in between SU-8 and PMMA on PET substrate.



Figure 3.1 PET with octadecagon shape

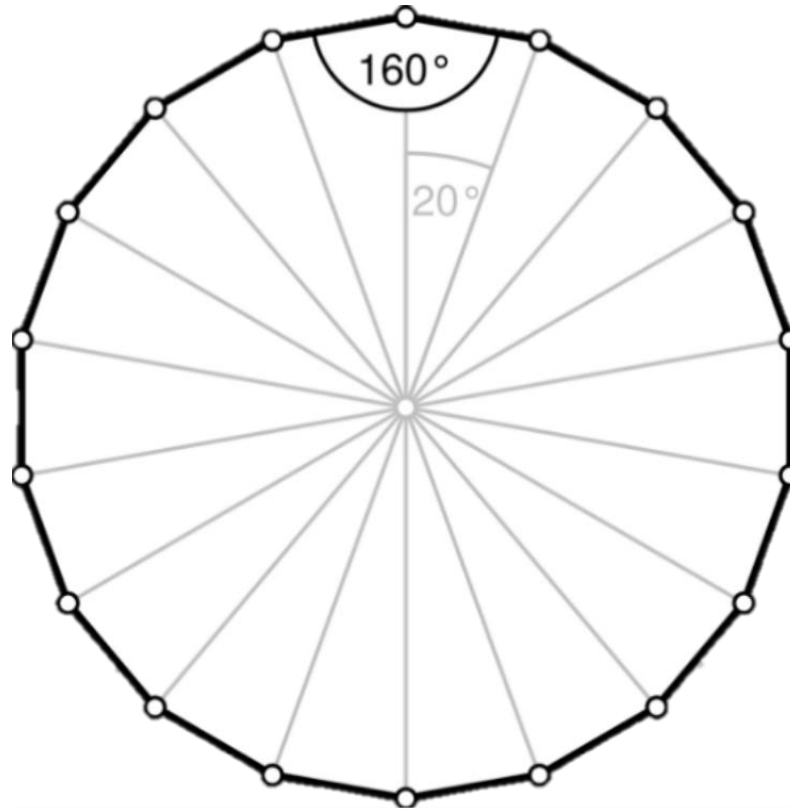


Figure 3.2 Schematic diagram of PET with octadecagon shape

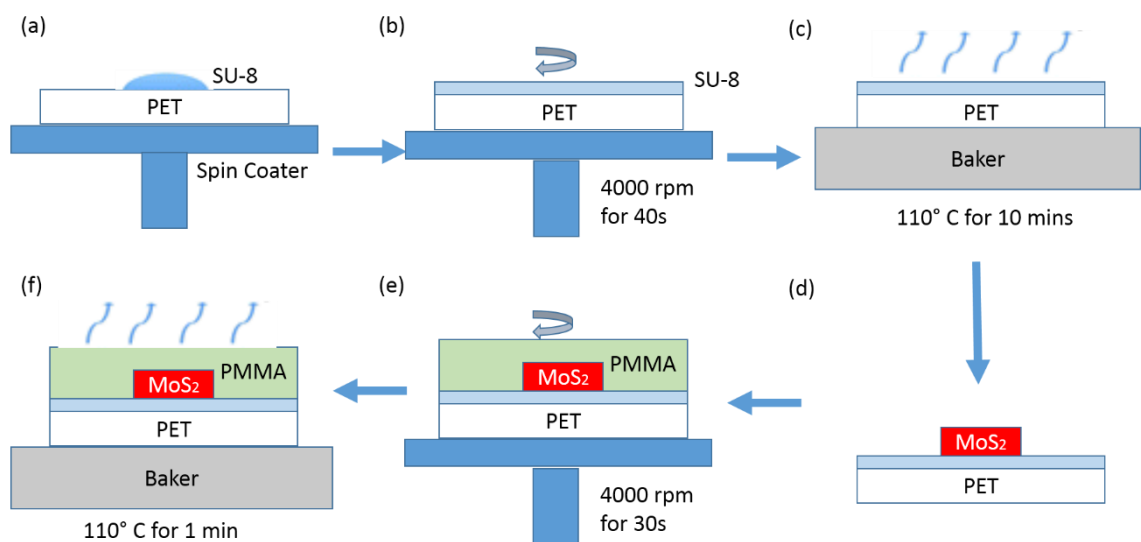


Figure 3.3 Schematic diagrams showing the fabrication process of MoS₂ encapsulated in between SU-8 and PMMA on PET substrate (a-b) Spin coating of SU-8 (c) Baking process (d) Transferring MoS₂ on top of PET (e) Spin coating of PMMA (f) Baking process (Not drawn to scale)

3D printer was used to build rectangular moulds of different sizes as shown in Figure 3.4. Those moulds were used to induce strain onto the PET substrate. Different strains from 1% up to 8% were induced to the PET substrate.



Figure 3.4 Moulds built by 3D printer

PET substrate was placed in between the gaps of the 3D mould, and the sample sitting on PET substrate was measured by Raman spectroscopy at different applied strains as shown in Figure 3.5. Six Raman spectra were obtained for each strain level and an average Raman shift for each peak was calculated. After Raman measurement in a specific uniaxial strain, PET substrate would be placed on a flat surface for one day to release its strain. In the next day, the uniaxial strain would be applied on the PET substrate with a 20° rotation with respect to previous measurement. Raman measurements were carried out from 0° rotation up to 180° rotation. Encapsulated MoS_2 with different thicknesses were measurement in this work to compare their respond. All the room temperature Raman spectra were measured with a 100x objective lens with

numerical aperture (NA) of 0.9. The diffraction grating was set as 1800 mm^{-1} . The power of 488nm laser was attenuated to $50 \mu\text{W}$ to avoid the possible localized heating effect.

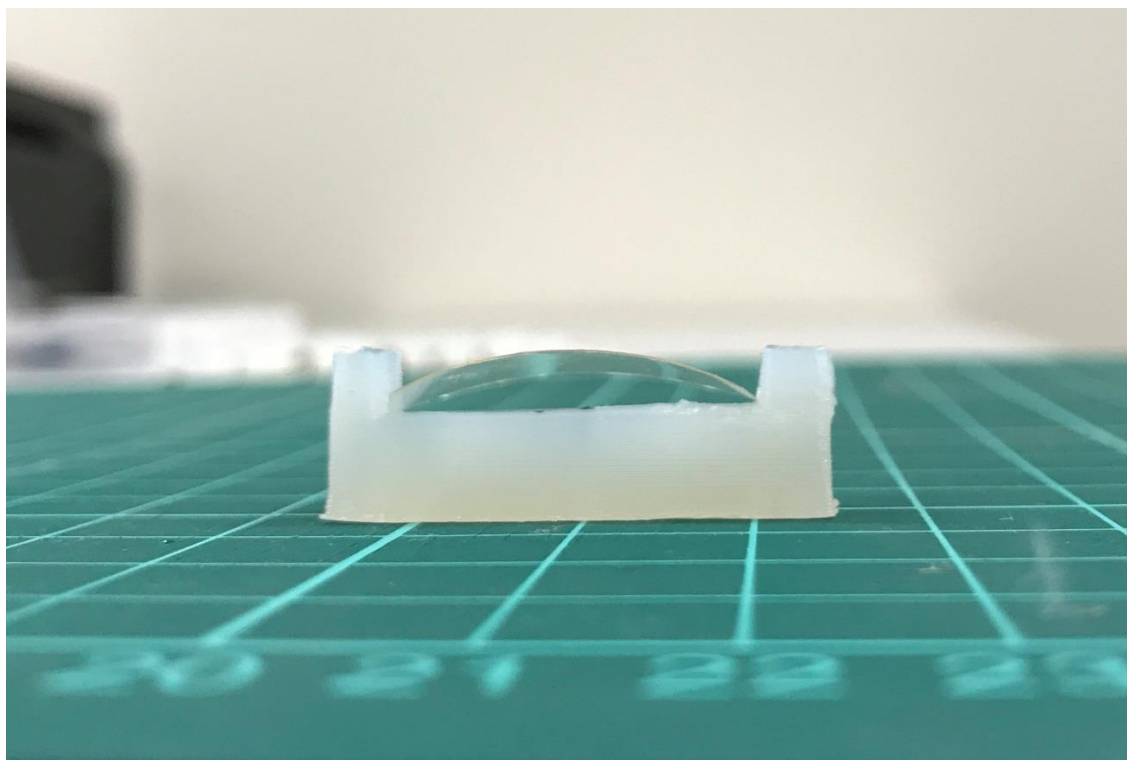


Figure 3.5 PET substrate embedded in between 3D mould

3.1.2. FeTe

The FeTe single crystal was purchased from 2D Semiconductors based in the United State. And its composition was confirmed by using secondary ion mass spectrometry (SIMS). FeTe was mechanically exfoliated to silicon substrate with 300 nm silicon dioxide. Optical microscopy was used to locate FeTe. Furthermore, some basic characterizations were done by using Atomic Force microscopy (AFM) and Raman Spectrometry. Measurements of Raman spectra were carried out by using Horiba Jobin Yvon HR800 Raman system. An external linear polarized diode pumped solid state laser of 488nm was utilized to excite the sample. 100 x objective lens with NA of 0.9 was used to focus the laser onto the sample with a spot size of roughly $1.0 \mu\text{m}$ at room temperature.

The diffraction grating was set as 1800 mm^{-1} . The power of the incident laser on the sample was attenuated to $50 \mu\text{W}$ to avoid the possible localized heating effect and oxidation from the solid-state laser [109].

3.2. Raman Spectra in different strained direction of MoS_2

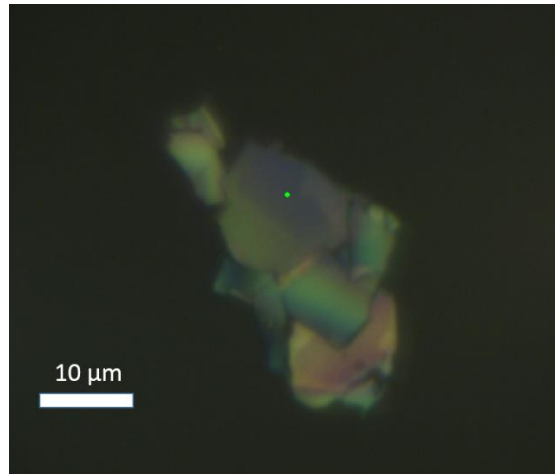


Figure 3.6 Optical image of the encapsulated bulk MoS_2 on PET substrate without applied uniaxial strain

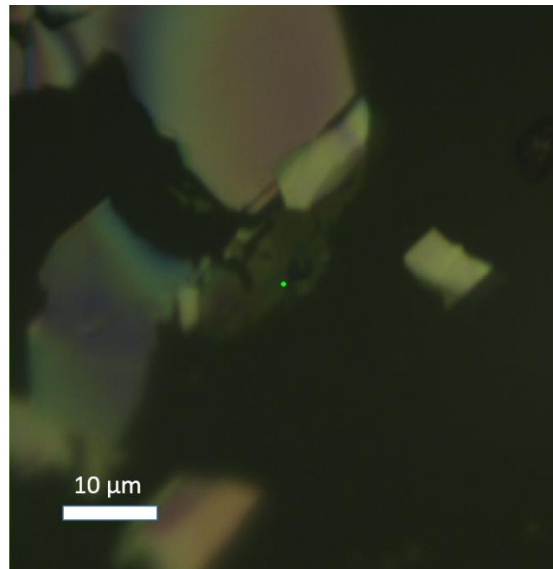


Figure 3.7 Optical image of the encapsulated quadrilayer MoS_2 on PET substrate without applied uniaxial strain

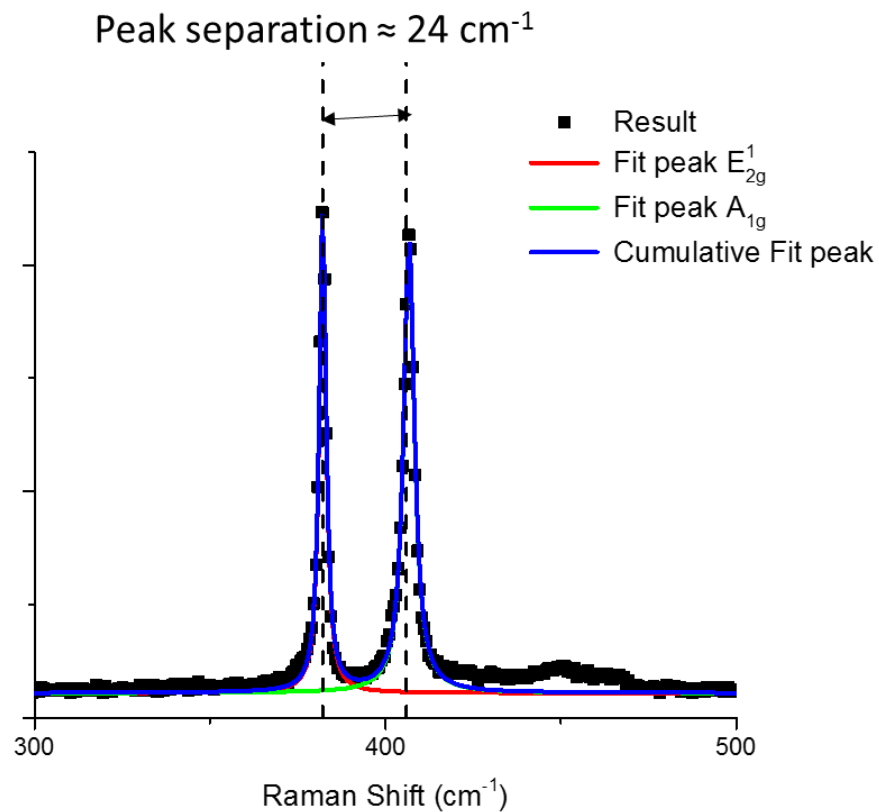


Figure 3.8 Raman spectra of the encapsulated quadrilayer MoS_2 on PET substrate without applied uniaxial strain

Optical microscopy was first used to allocate different thicknesses of MoS_2 on PET substrate. Figure 3.6 and Figure 3.7 present the optical image of the bulk MoS_2 which was around 100nm and quadrilayer MoS_2 on PET substrate without applied uniaxial strain. Number of layer was then identified by measuring their Raman spectra. A typical Raman spectrum of encapsulated quadrilayer MoS_2 on PET substrate without applied uniaxial strain is shown in Figure 3.8. Lorentzian peak fitting was employed to fit the feature peaks E_{2g}^1 and A_{1g} of MoS_2 . The Raman peak separation was roughly 24 cm^{-1} which corresponding to four layer/ quadrilayer [42]. For the bulk MoS_2 , Raman separation of its feature peaks was roughly 25 cm^{-1} which was similar to report value [42].

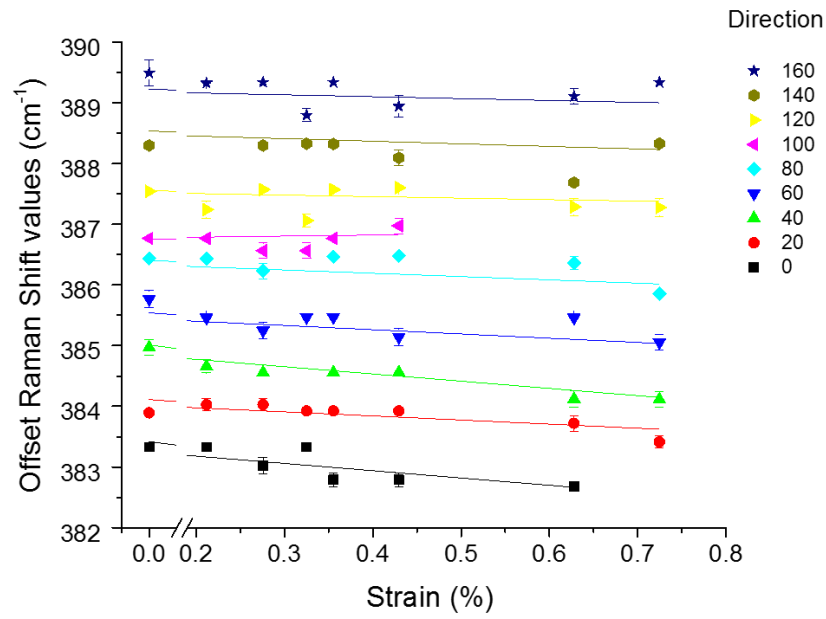


Figure 3.9 Raman shift of E_{2g}^1 modes of the bulk MoS_2 as a function of the applied strain for different uniaxial strain directions together with linear fitting

Direction / degree	Raman Shift rate ($\text{cm}^{-1}/\text{Strain}$)
160	-0.31
140	-0.43
120	-0.25
100	0.18
80	-0.54
60	-0.7
40	-1.19
20	-0.67
0	-1.20

Table 2 Raman shift rate of E_{2g}^1 modes of the bulk MoS_2 for different uniaxial strain directions

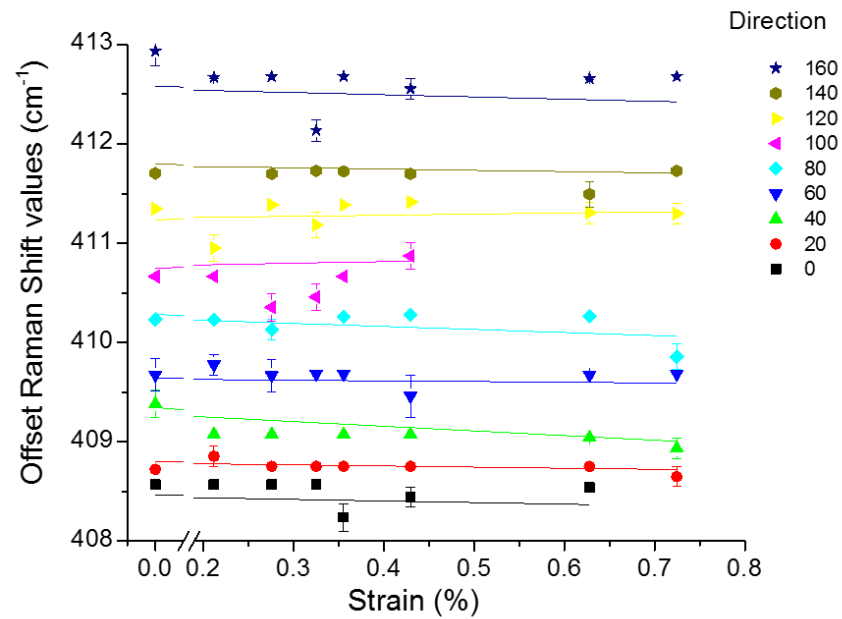


Figure 3.10 Raman shift of A_{1g} modes of the bulk MoS_2 as a function of the applied strain for different uniaxial strain directions together with linear fitting

Direction / degree	Raman Shift rate (cm ⁻¹ /Strain)
160	-0.22
140	-0.13
120	0.11
100	0.17
80	-0.31
60	-0.07
40	-0.47
20	-0.11
0	-0.16

Table 3 Raman shift rate of A_{1g} modes of the bulk MoS_2 for different uniaxial strain directions



Figure 3.9 and Figure 3.10 shows the Raman shift of E_{2g}^1 and A_{1g} modes of the bulk MoS_2 as a function of the applied strain for different uniaxial strain directions together with linear fitting respectively. Table 2 and Table 3 are the Raman shift rate of E_{2g}^1 and A_{1g} modes of the bulk MoS_2 for different uniaxial strain directions respectively. Positive sign in the table indicates red shift of the vibrational mode and negative sign means blue shift. For E_{2g}^1 mode, only applied uniaxial strain directions from 0° to 80° had a Raman shift rate that greater than $0.5 \text{ cm}^{-1}/\text{strain}$. Raman shift rate E_{2g}^1 of had the biggest when the uniaxial strains were applied along 0° and 40° . On the other hand, it only happened to A_{1g} when the strain direction was 0° . Others including those Raman shift rate in A_{1g} mode, however, had a Raman shift rate smaller than 0.5 cm^{-1} . The resolution of our Raman system is 0.5 cm^{-1} . Thus, the changes in those bulk MoS_2 might be due to the system error.

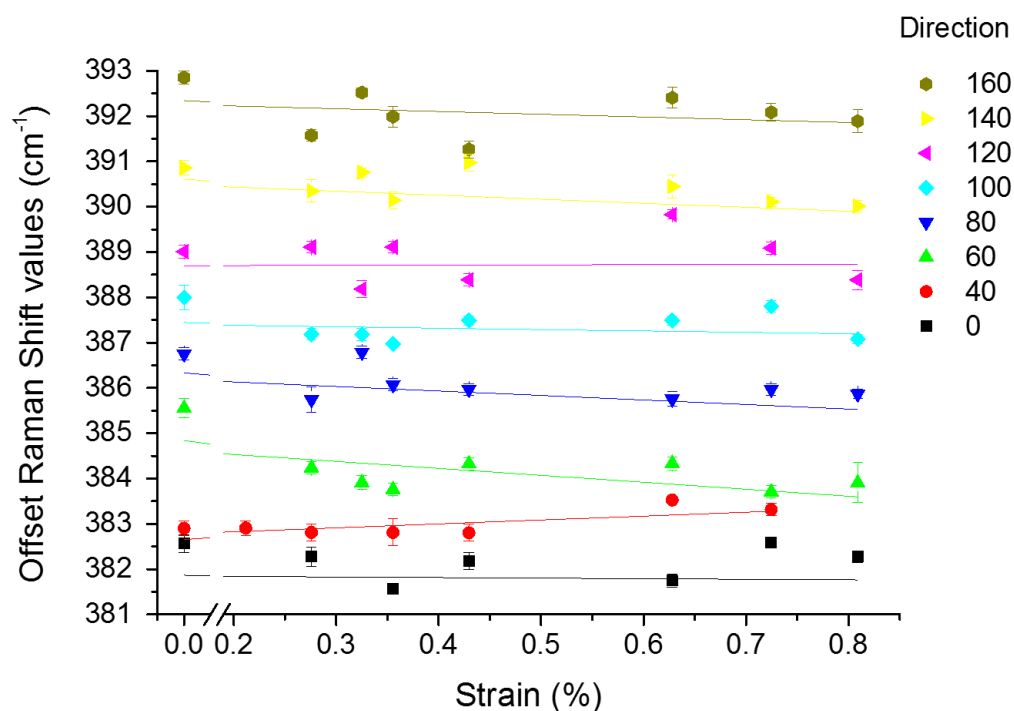


Figure 3.11 Raman shift of E_{2g}^1 modes of the quadrilayer MoS₂ as a function of the applied strain for different uniaxial strain directions together with linear fitting

Direction / degree	Raman Shift rate (cm ⁻¹ /Strain)
160	-0.60
140	-0.89
120	0.051
100	-0.31
80	-1
60	-1.54
40	0.86
0	-0.13

Table 4 Raman shift rate of E_{2g}^1 modes of the quadrilayer MoS₂ for different uniaxial strain directions

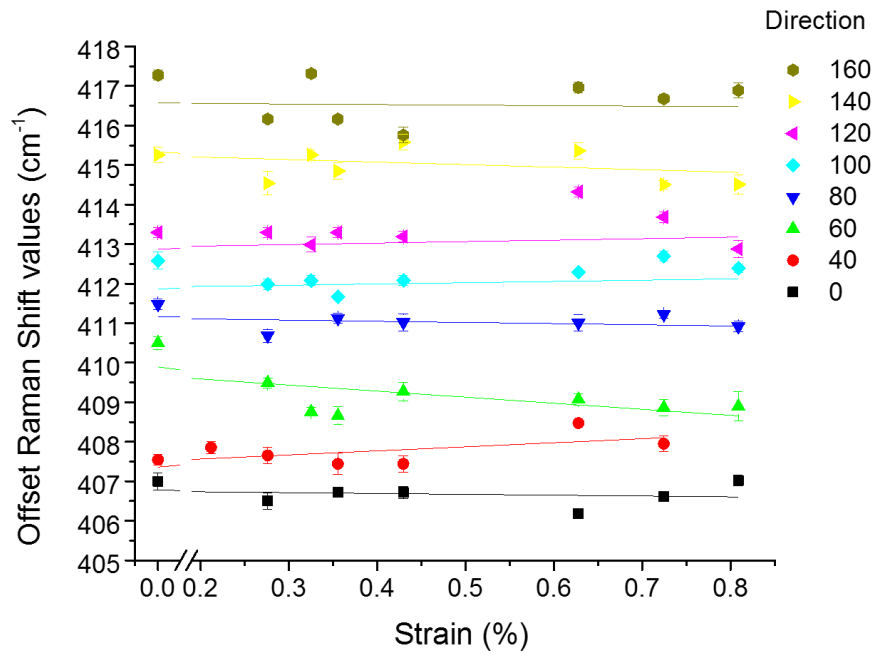


Figure 3.12 Raman shift of A_{1g} modes of the quadrilayer MoS_2 as a function of the applied strain for different uniaxial strain directions together with linear fitting

Direction / degree	Raman Shift rate ($cm^{-1}/Strain$)
160	-0.13
140	-0.64
120	0.38
100	0.32
80	-0.30
60	-1.53
40	1.03
0	-0.21

Table 5 Raman shift rate of A_{1g} modes of the quadrilayer MoS_2 for different uniaxial strain directions



The Raman shifts of E_{2g}^1 and A_{1g} modes of the quadrilayer MoS_2 as a function of the applied strain for different uniaxial strain directions together with linear fitting are shown in Figure 3.11 and Figure 3.12 respectively. The Raman shift rate of E_{2g}^1 and A_{1g} modes of the quadrilayer MoS_2 for different uniaxial strain directions are presented in Table 4 and Table 5 respectively. For Raman shift rate of A_{1g} mode of the quadrilayer MoS_2 in different applied uniaxial strain, most of them had a Raman shift rate higher than $0.5\text{cm}^{-1}/\text{strain}$ especially in the direction of 60° , both E_{2g}^1 and A_{1g} modes have a red shift rate that around 1.5. When a further 60° is applied onto it, which is around 120° , E_{2g}^1 and A_{1g} modes become very insensitive to the applied uniaxial strain. This finding perhaps implies that applied uniaxial strain at 60° is applying along to the armchair direction of quadrilayer MoS_2 , which explains that why in this direction it has a very high Raman shift rate for both E_{2g}^1 and A_{1g} modes. Furthermore, when a further 60° angle is applied, the uniaxial strain has attributed from armchair direction to the zigzag direction, which is the reason why it becomes relatively not sensitive to the applied uniaxial strain. It has also been reported that the anisotropic thermoelectric behaviour in armchair and zigzag direction can behave differently [110]. Therefore, the different Raman shift rate in armchair and zigzag direction can be used as a method to determine the crystalline orientation direction of exfoliated samples.

3.3. Raman Spectra for different thicknesses of FeTe



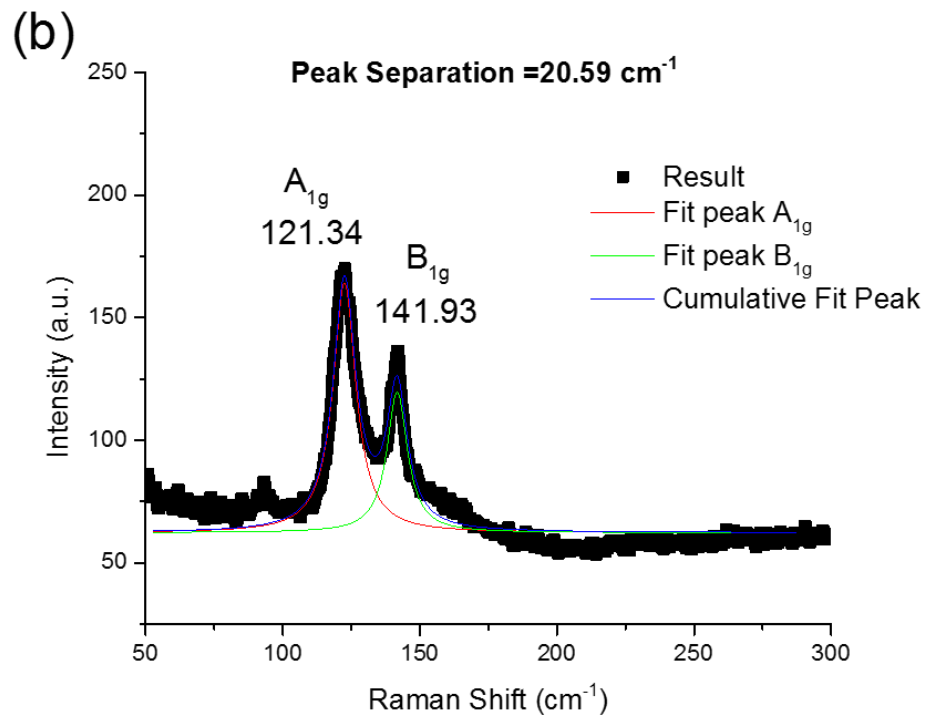


Figure 3.13 Basic Raman Study of FeTe. (a) Optical image of bulk FeTe (b) Raman spectra of bulk FeTe

Figure 3.13 (a) presents an optical image of FeTe for Raman study. As shown in Figure 3.13 (a), FeTe flakes with different thicknesses and various colour contrast of the sample were observed. Since mechanical exfoliation was used, the crystal orientation FeTe sample was not able to be predicted. Optical microscopy was used to locate the FeTe samples. Black spot in Figure 3.13 (a) is the position where Raman spectrum was measured. As shown in Figure 3.13 (b), peaks around 120cm⁻¹ and 140 cm⁻¹, corresponding to its vibrational modes A_{1g} and B_{1g} respectively, are observed. Different from MoS₂ [42], relationship between Raman peak separation and number of thickness of FeTe has not been reported. If a relationship can be established, it would save time for doing AFM. For bulk FeTe the Raman peak separation between A_{1g} and B_{1g} is about 20 cm⁻¹.

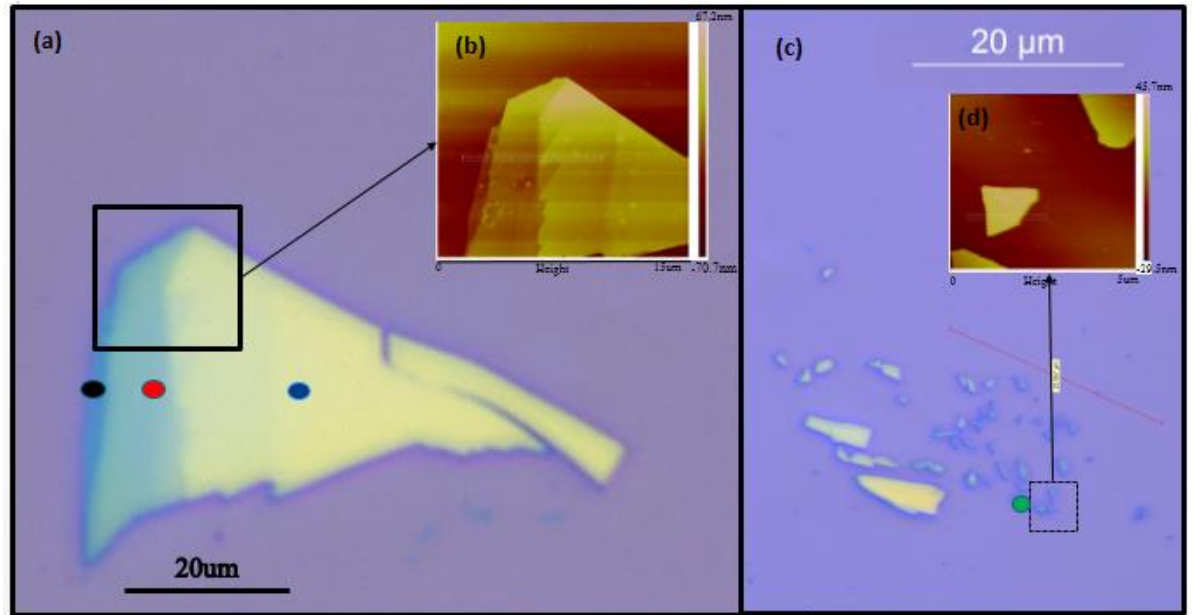


Figure 3.14 Optical images of thin FeTe. (a) Optical image of thin FeTe (b) AFM image (c) Optical image of thin FeTe (d) AFM image

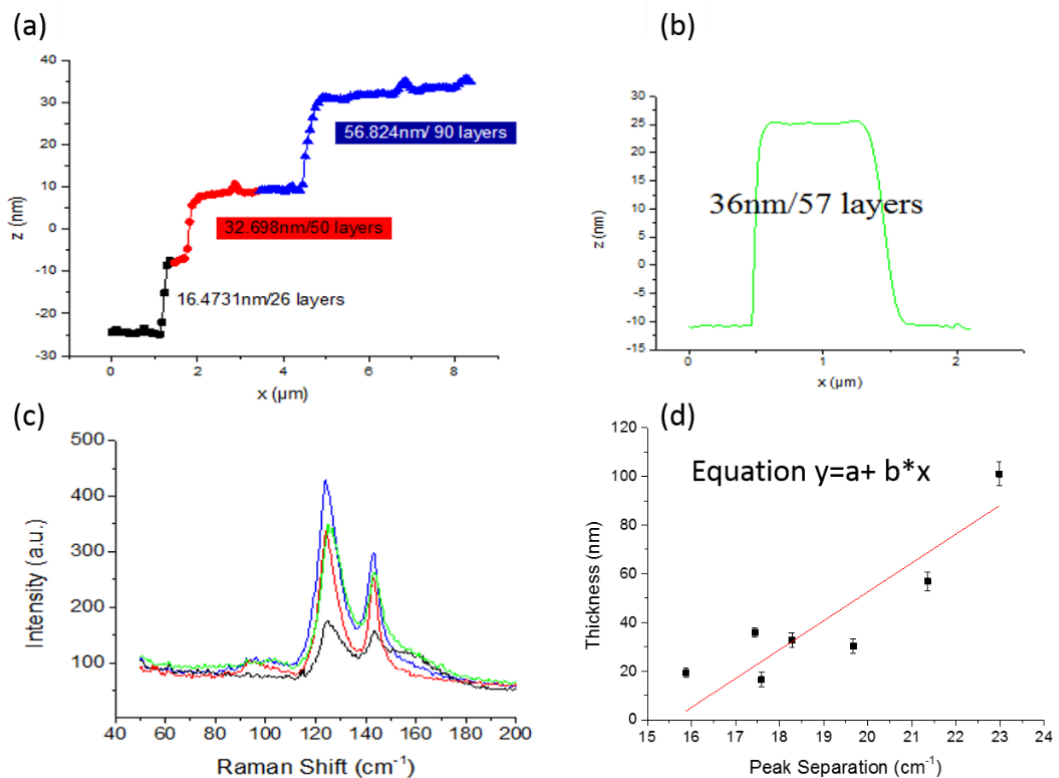


Figure 3.15 Characterization of thin FeTe. (a) step height measurement of the thin FeTe (b) step height measurement of another thin FeTe (c) Raman spectra of thin FeTe (d) Graph of Thickness of FeTe against peak separation.

Figure 3.14 presents the optical image of thin FeTe together with its AFM image. Figure 3.15 shows the characterization result of thin FeTe. Coloured spots in Figure 3.14 (a) and (c) represent the positions where Raman spectra were measured. The coloured spots in Figure 3.14 (a) and (c) were corresponding to Raman spectra of same colour in Figure 3.15 (a), and (c) respectively. In Figure 3.15 (c) consists of Raman spectra of these four positions that corresponding to different thickness of FeTe. Both vibrational modes A_{1g} and B_{1g} were obtained by using Lorentzian fitting. As the findings in Figure 3.15 (c) indicates the thinnest layer in Figure 3.14 (a) (black spot) had a broad Raman Spectrum. A possible explanation for this result is the lateral size of the thinnest layer part is smaller than the spot size of the Raman Spectroscopy, the other signals near to the thinnest area of FeTe are also collected.

Graph of thickness of FeTe against peak separation was plotted to study the thickness dependence of FeTe to its Raman spectra as shown in Figure 3.15 (d). As is shown Figure 3.15 (d), the peak separation of FeTe does vary corresponding to its thickness. This kind of changes is also observed in other 2D materials such as MoS_2 , WS_2 and etc. [42, 111]. A linear change of Raman shift can be observed in Figure 3.15 (d). However, in order to improve the accuracy of the results, Raman spectroscopy with better spatial resolution will be required.

3.4. Summary

In summary, comprehensive study of the anisotropic strain response in Raman modes of different thicknesses MoS_2 using a modified bending technique has been carried out. The Raman shift rates of the E_{2g}^1 and A_{1g} modes of the bulk MoS_2 , are not sensitive to the



different applied strain directions. On the other hand, when the applied strain direction was applied to the quadrilayer MoS₂ 60 °with respect to the original direction, it had a highest Raman shift rate among the others for both E_{2g}¹ and A_{1g} modes. When additional 60 °was added (crystalline direction changes from armchair to zigzag direction), Raman shift rate had become very small. Based on the anisotropic strain response in E_{2g}¹ and A_{1g} modes for mono or few layer MoS₂, this work shows the possibility of a new simply method to identify the crystalline orientation of thin MoS₂ using the strained exfoliated MoS₂ and the Raman spectroscopy. On the other hand, a basic optical characterization of different thickness of exfoliated FeTe was studied in this work. FeTe samples were prepared by using mechanically exfoliation and Raman spectra were carried to investigate the relationship between thickness and Raman shift. The result shows that the Raman spectra for different thicknesses of FeTe change corresponding to its thickness.



4. Electrical properties of 2-dimensional Materials

This chapter provides an overview about electrical properties of different 2D materials. It is divided into four sections: (i) experimental setup, (ii) effect of various electrode preparation processes on As_2S_3 , (iii) study of I-V characteristic of P-N junction and iv) superconductivity in iron-based 2D materials. At first, whether the electrode preparation process using e-beam lithography will bring any damage to As_2S_3 , a 2D material with low melting point, was studied. Raman Spectra were obtained after different processes such as covered by PMMA, treatments after E-beam lithography and E-beam evaporation. Besides, the I-V characteristic of the p-n junction formed by using p- As_2S_3 and n- MoS_2 is presented. At the end of this chapter, temperature dependent resistance of FeSe and FeTe are displayed in order to observe the superconductivity in these iron-based 2D materials.

4.1. Experimental Setup

Silicon wafers covered with 300nm thermally grown silicon dioxide were used as substrate. All the substrates were cleaned by standard procedure with acetone and ethanol. The alignment mark was made by pre-coated a layer of AZ5214 photoresist on the substrate and then patterned by the assist of photolithography. It was then developed and deposited by using Magnetron sputtering. After the deposition process, it was lift-off by using acetone. Figure 4.1 shows the alignment mark in the silicon substrate. The thickness of each alignment mark was Au (50nm)/ Ti (5nm) in our

experiment. These alignment marks were used to locate the target sample more easily in optical microscopy as well as e-beam lithography.



Figure 4.1 Silicon Substrate Alignment Mark

The As_2S_3 , FeTe and FeSe single crystals were purchased from 2D Semiconductors based in the United State. As_2S_3 crystal was then mechanically exfoliated and put on top of the marked Si substrate. Then Raman spectra were carried out after patterned by e-beam lithography and deposited with Au (50 nm)/ Ti (5 nm) electrode. These results were compared with another As_2S_3 sample of similar thickness which was exposed under e-beam for 15 secs. All the Raman spectra were measured by a laser line 488 nm of power at 15 μW with a 100x objective lens, NA of 0.9. The laser spot onto the sample had a spot size around 1.0 μm .

The configuration of the p-n junction was P- As_2S_3 / N- MoS_2 , As_2S_3 was prepared by mechanically exfoliated onto the silicon substrate. MoS_2 was then transferred on top of As_2S_3 by using dry transfer method. All the I-V characterize curves were measured



using a two-point measurement setup including a Keithley 2400 meter with our own LabView program. I-V characterize curves were measured under different circumstances. For example, measurements were done when p-n junction was illuminated with and without white LED at low temperature. Raman system was used to characterize the structural properties of the samples.

FeTe was also mechanically exfoliated and transferred on top of silicon substrate. Then it was immediately coated by PMMA to avoid degradation in the ambient. Au 50 nm/ Ti 5 nm electrodes were fabricated by using e-beam lithography, e-beam evaporation and lift-off method. Graphene was dry transferred on top of the FeTe as a protection layer. Raman system was used to identify the samples. The four-point resistivity measurements were obtained at a slow heating and cooling rate of 5K/min from 300K to 50K and 1K/min from 50K to 2K using a Physical Properties Measurement System (PPMS).

FeSe was prepared differently from others. Four electrodes (Au 50 nm/ Ti 5 nm) were pre-fabricated by using e-beam lithography, e-beam evaporation and lift-off method. FeSe was dry transferred on top to those electrodes and covered immediately by PMMA. The four-point resistivity measurements were obtained at a slow heating and cooling rate of 5K/min from 300K to 50K and 1K/min from 50K to 2K by using a Physical Properties Measurement System (PPMS).

4.2. Effect of Electrode Preparation process on As_2S_3

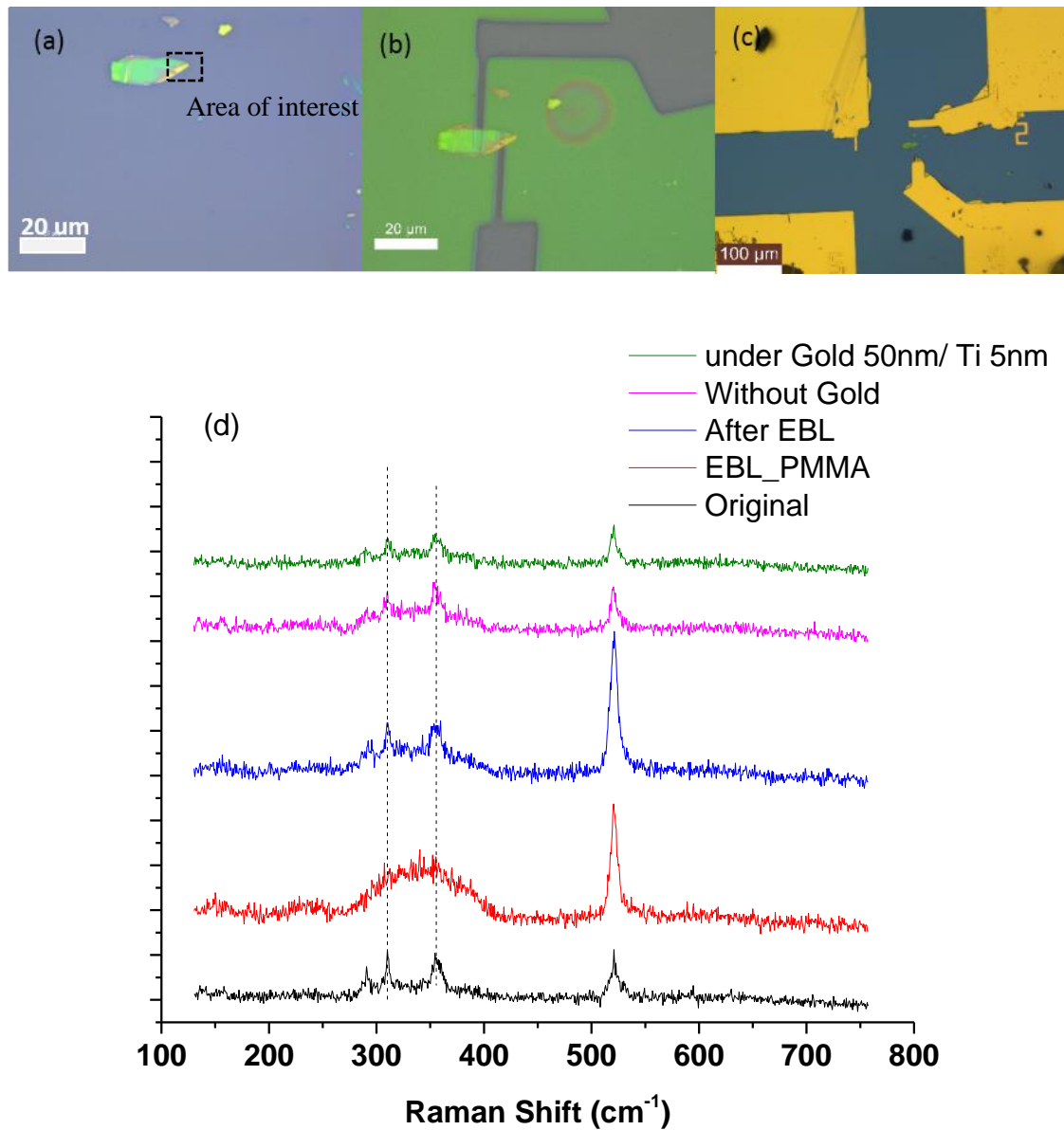


Figure 4.2 (a) Optical image of Original As_2S_3 (b) Optical image of As_2S_3 after E-Beam Lithography (c) Optical image of As_2S_3 after E-beam Evaporation (d) Raman spectra with respect to original, part cover under PMMA, part after E-Beam Lithography, part cover by gold and without gold of As_2S_3

Figure 4.2 (a), (b) and (c) show the optical images of original As_2S_3 , after it was patterned by using E-beam lithography and after it was deposited by using E-beam evaporation respectively. E-beam lithography can induce heat up to 300K on to the



sample and this might be able to damage the sample [112]. E-beam evaporation, on the other hand, does not induce any heating on the sample as shown in our temperature detector inside the e-beam chamber in. As shown in Figure 4.2 (a), (b) and (c), no physical damage can be observed under their optical images. As shown in the Raman spectra in Figure 4.2(d), two feature peaks can be observed at around 310 cm^{-1} and 355 cm^{-1} . As_2S_3 can be characterized by peak at $\sim 355\text{ cm}^{-1}$ which is attributed to the symmetric stretching vibrational mode of $\text{AsS}_{3/2}$ pyramids. Besides this strong band, there is an additional feature at approximately 310 cm^{-1} , which is assigned to the asymmetric stretching modes of $\text{AsS}_{3/2}$ pyramids[113]. As shown in Figure 4.2(d), the two feature peaks are still able to be observed in all the Raman spectra. This finding perhaps indicates that electrode preparation does not have any structural influence on As_2S_3 which has low melting point.

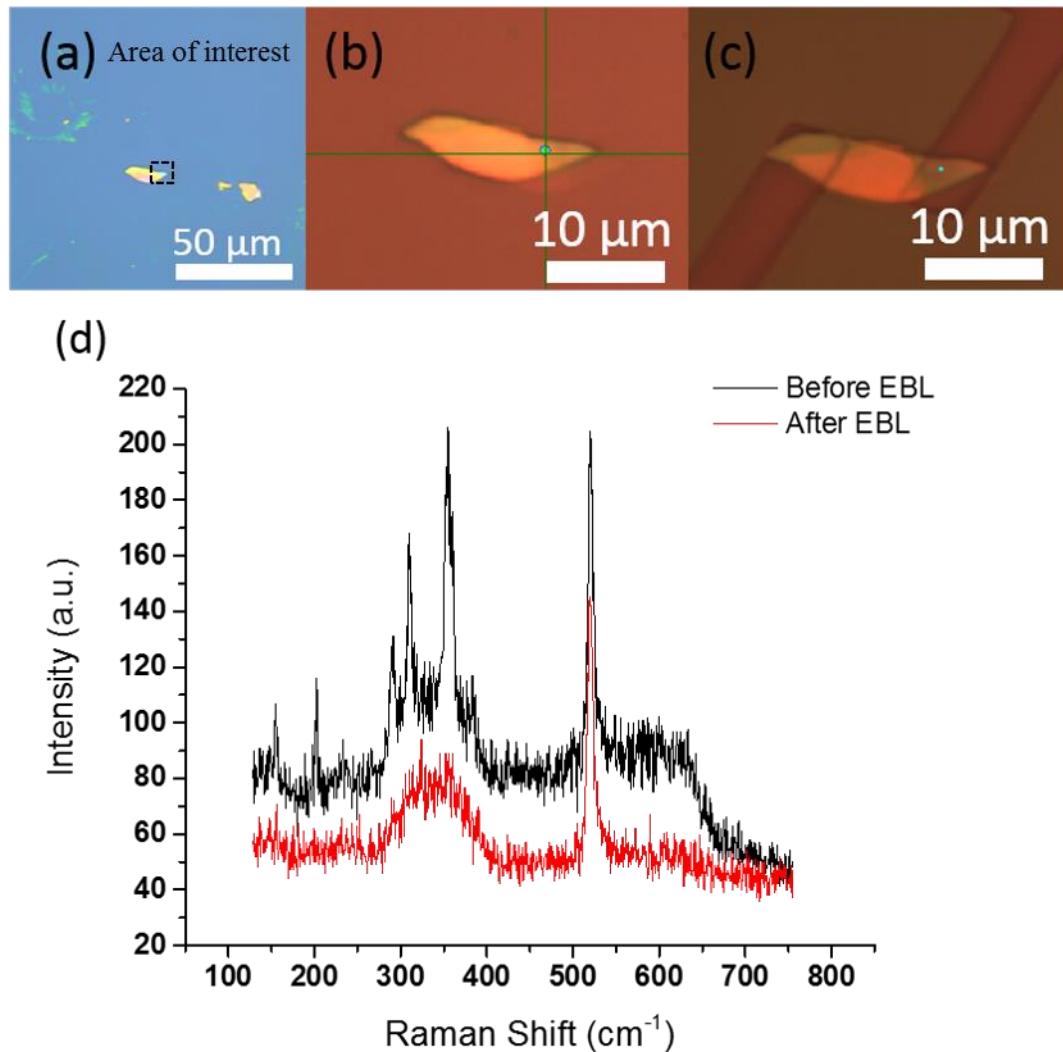


Figure 4.3 (a) Optical image of Original As_2S_3 (b) Optical image of As_2S_3 under Raman microscopy (c) Optical image of As_2S_3 after E-beam lithography (d) Raman spectra with respect to before and after E-Beam Lithography.

Figure 4.3 (a), (b) and (c) show the optical images of original As_2S_3 , optical image of As_2S_3 under Raman microscopy and optical image of As_2S_3 after e-beam lithography. After exposed under e-beam lithography for 15 sec, the colour of the exposed sample under e-beam lithography had changed as shown in Figure 4.3 (b) and (c). It indicates that if As_2S_3 exposes under e-beam lithography more than 15 secs the sample will have some structural changes which also can be observed in its Raman spectra as shown in Figure 4.3 (d) as the feature peaks cannot be observed after the e-beam lithography.

4.3. Study of I-V characteristic of P-N junction

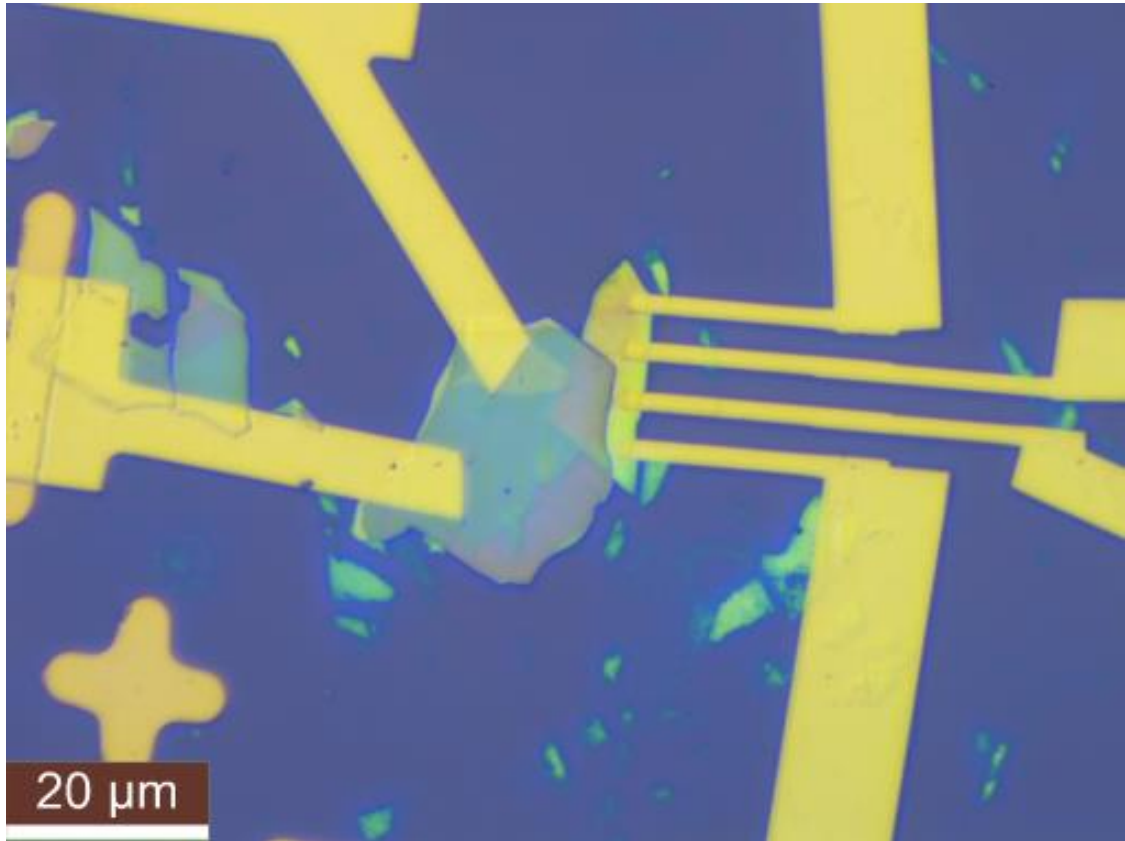


Figure 4.4 Optical image of PN junction formed by As_2S_3 and MoS_2

In Figure 4.4, the big and translucent sample that connected by two electrodes is bulk MoS_2 which has been transferred on top of bulk As_2S_3 using dry transfer method. We believe that a then a p-n junction was formed by using these two 2D materials as the MoS_2 is a n-type semiconductor while As_2S_3 is a p-type semiconductor.

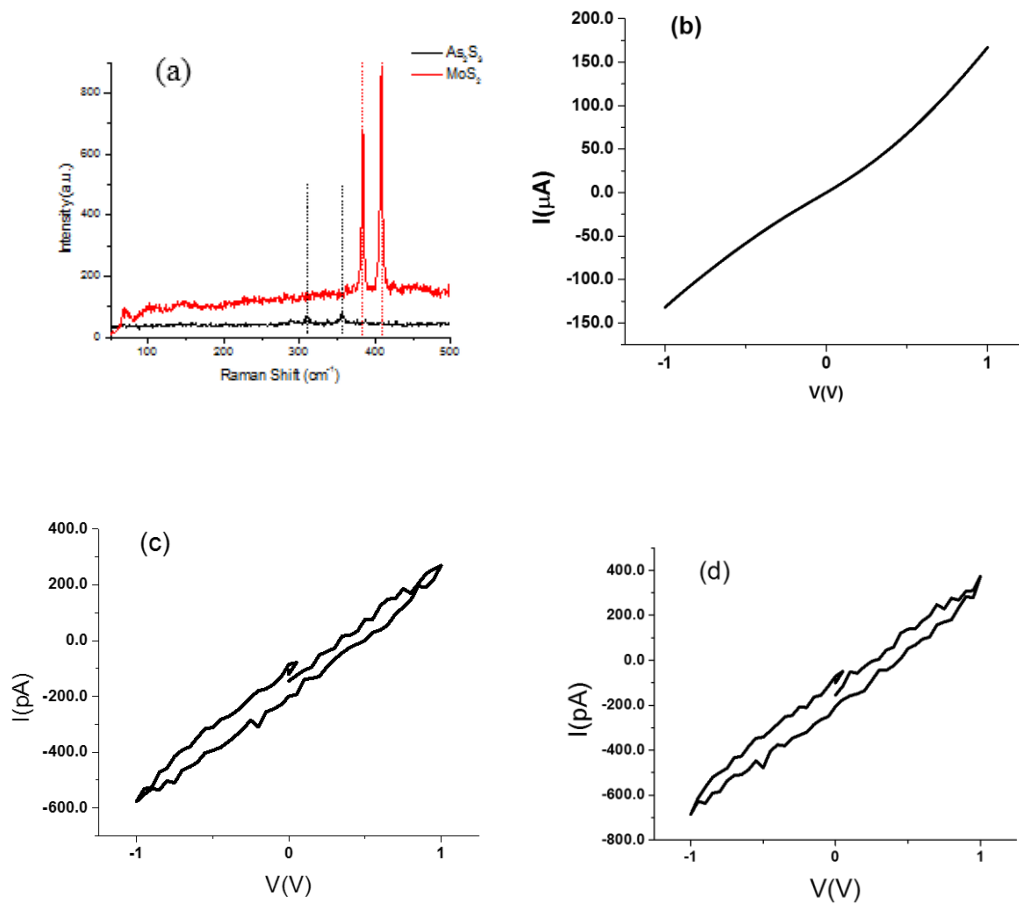


Figure 4.5 (a) Raman Spectra of As₂S₃ and MoS₂ (b) I-V characteristic curve of MoS₂ (c) I-V characteristic curve of As₂S₃ (d) I-V characteristic curve of p-n junction

Raman measurement was carried out to confirm the materials on top of Silicon substrate which is shown in Figure 4.5 (a). As shown in Figure 4.5 (a), both feature peaks for MoS₂ and As₂S₃, red and black dot lines, were able to be observed. I-V characteristic measurements were conducted on MoS₂ and As₂S₃ respectively. Figure 4.5 (b), (c) and (d) show the I-V characteristic curves of MoS₂, As₂S₃ and p-n junction respectively. As shown in Figure 4.5 (b), MoS₂ was much more conductive than As₂S₃, as shown in Figure 4.5(c). Currents in MoS₂ and As₂S₃ were at the range at order of 10⁻⁶ and 10⁻¹² respectively. Converting it by using Ohm's law, the resistance of As₂S₃ is six order of magnitude higher



than MoS₂. As observed in Figure 4.5 (d), the current of the p-n junction had the smallest current among the others with similar resistance large as there is As₂S₃. This probably reflects the fact that why p-n junction of p-As₂S₃ and n-MoS₂ had the least conductive among the others. Perhaps this finding also indicates that the low mobility in As₂S₃ has caused the high resistance in the result. On the other hand, instead of showing p-n junction result in I-V characteristic curve, it shows an Ohmic contact behaviour which might also because of the low conductivity in p-As₂S₃.

A further analysis was studied to this junction under different conditions such as illuminating under white LED and low temperature environments. There were no changes in the I-V characteristic of MoS₂ in the two circumstances. For As₂S₃ and p-n junction, however, reacted differentially under those circumstances [56].

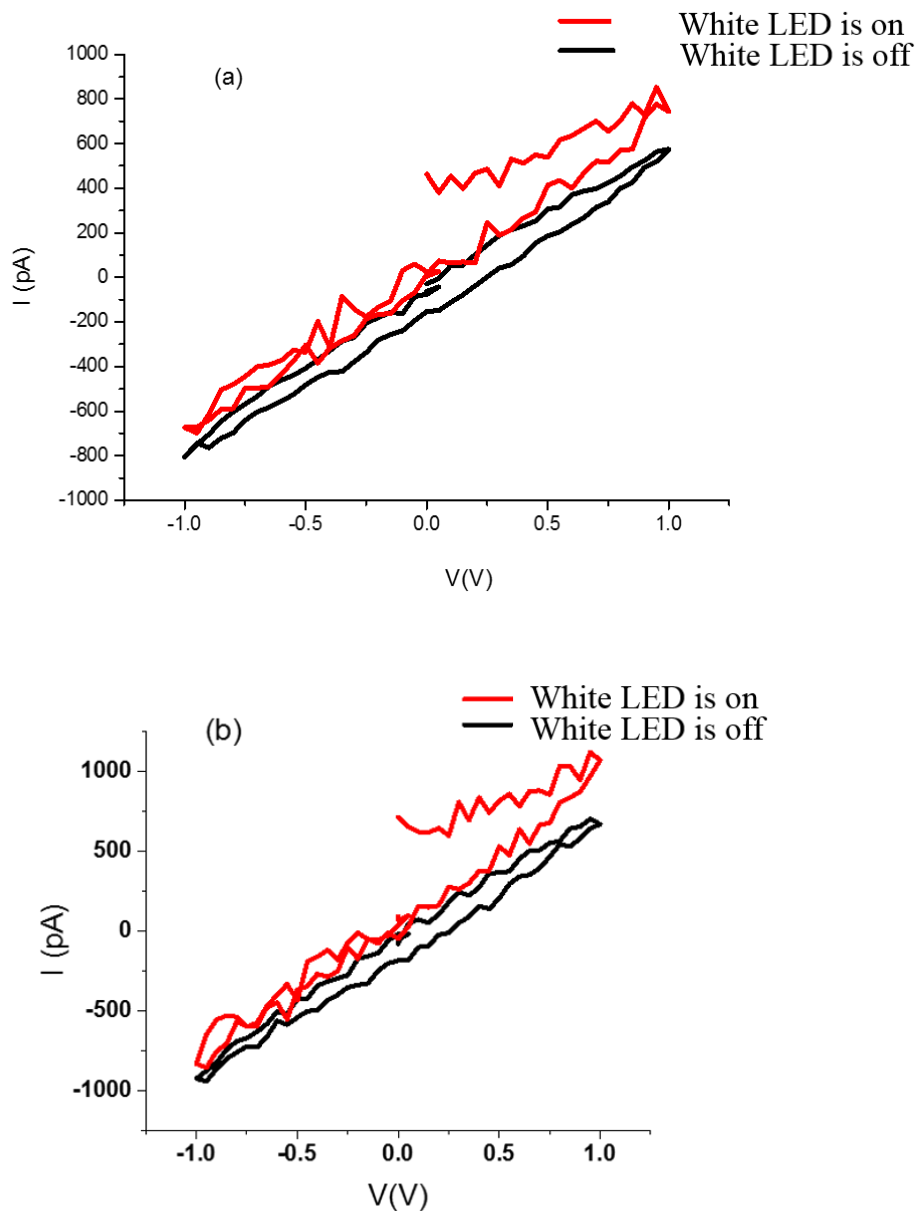


Figure 4.6 (a) I-V characteristic response of As_2S_3 exposed to white LED (b) I-V characteristic response of p-n junction exposed to white LED

Inset of Figure 4.6 shows the respond of As_2S_3 and p-n to the present of white LED. As shown in Figure 4.6 (a) and (b), the illumination of white LED would lead to a split in the IV curve which is a change when compare to the result when the white LED switched “OFF”. The reason that causing the split when the white LED “ON” is still

undetermined. As_2S_3 and p-n junction, generally, had become more conductive under the present of white LED. A possible explanation for its becomes more conductive by 15% is that As_2S_3 has a direct band gap around 2.2eV that illumination of white LED on to those samples has enhanced the hole mobility which lead it becomes more conductive[114]. Furthermore, the I-V characteristics of As_2S_3 and p-n junction were not responsive to applied low temperature (77 K)

4.4. Superconductivity in Iron-Based 2D materials

4.3.1. Iron Telluride (FeTe)

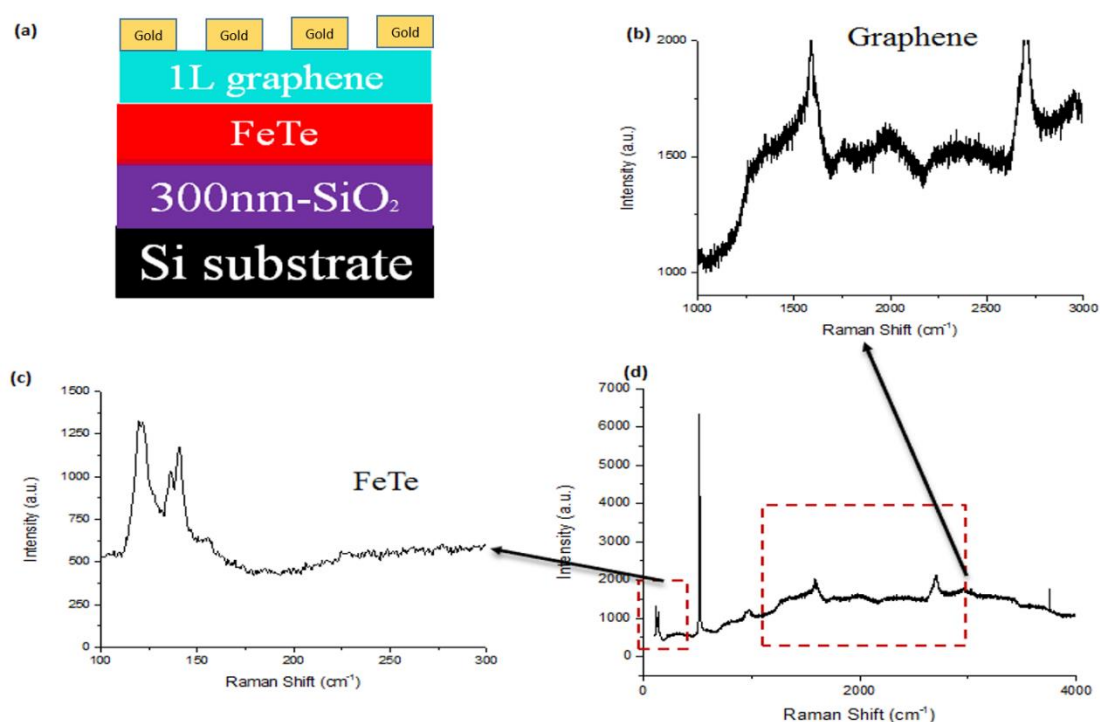


Figure 4.7 (a) Structural diagram of FeTe sample (b) Enlargement of Raman Spectrum from 1000 to 3000 cm^{-1} (c) Enlargement of Raman Spectrum from 100 to 300 cm^{-1} (d) Raman Spectrum of FeTe after covered by Graphene.

Thin FeTe layer was prepared by mechanical exfoliation. It was transferred to silicon substrate and then Graphene was transferred on top of FeTe. Figure 4.7 (a)

shows the schematic diagram of FeTe sample in this experiment, and Raman measurement was performed to verify the sample. It is noticed from Figure 4.7 (d) that both feature peaks from Graphene and FeTe were observed, indicating indicated that Graphene had been successfully transferred on top of the FeTe. Tetragonal FeTe has a structure very analogous to superconducting FeSe [49]. However, FeTe only shows its superconductivity behaviour under high pressure or by chemical doping [51]. A transition around 80 K shows an anomaly change of resistivity due to its structural transition [51].

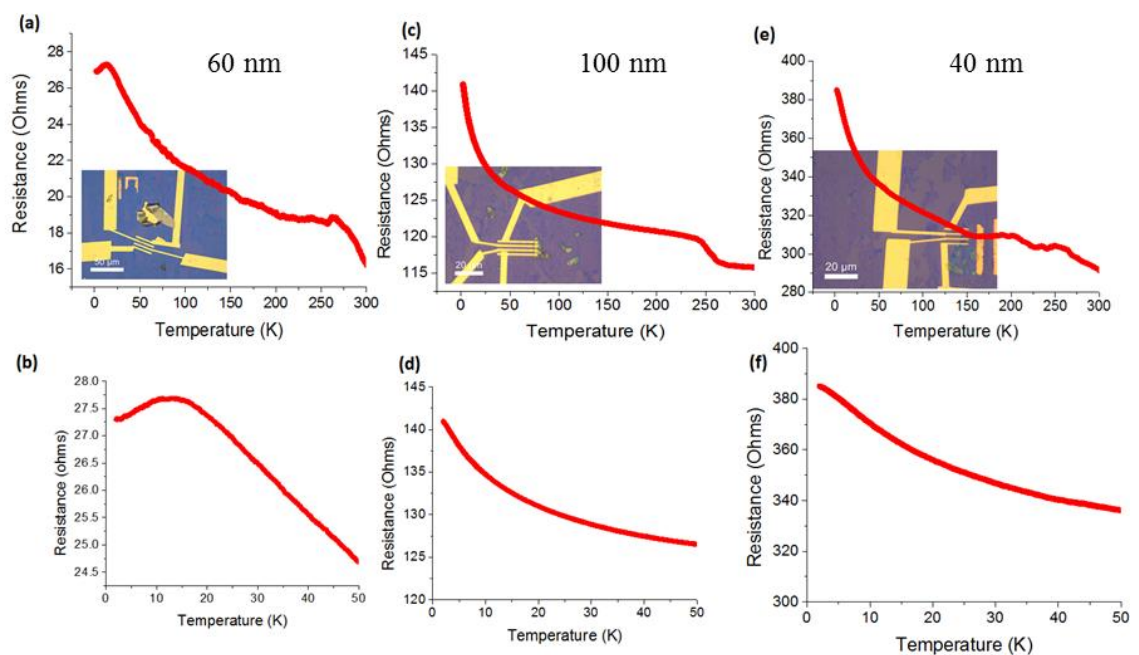


Figure 4.8 Temperature dependence of resistance for FeTe together with the enlargement image of the low temperature part

Figure 4.8 shows the temperature dependence of resistance for FeTe with different thicknesses which are roughly 60nm, 100nm and 40nm respectively. Figure 4.8 (b), (d), (f) are the enlargements of the low temperature part for Figure 4.8 (a), (c), (e) respectively.

As shown in in Figure 4.8 (a), it is noticed that a transition temperature around 11K is observed. Above the transition temperature, a semiconductor behaviour is identified and metallic behaviour is revealed below the transition temperature. This



transition was also observed in other researches' work[85]. The vast majority of people believe that it is due to structural change from tetragonal to orthorhombic phase. Other researchers, however, reported that the transition temperature was at $\sim 80\text{K}$ [85]. Even there was a transition observed in the resistance (Figure 4.8(a)), a perfect 2D superconductor without any offset could not be obtained. For other samples, transition temperature could not be observed up until 2K. This phenomenon may be attributed to the different thicknesses of FeTe. As shown in the optical images shown in Figure 4.8 (a), (c) and (e) the colour contrast in those images suggested that the difference in thickness. As it is expected to see a T_c around 9.1K, however it cannot be observed due the thickness of FeTe.

4.3.2. Iron Selenide (FeSe)

FeSe was prepared differently from FeTe because scientists believe that FeSe is highly sensitive to air environment i.e. it can be easily oxidized in air [115]. Electrodes, therefore, was pre-prepared on top of Silicon substrate then the FeSe was transferred on top of the electrodes immediately by using dry transfer method. Then, it was covered spontaneously by PMMA to avoid further contamination. As reported by Takano et.al, FeSe shows a structural phase transition at around 90K from tetragonal to orthorhombic phase, and it becomes superconductivity below $T_c \approx 8.5\text{K}$ [48]. Structural diagram of our FeSe sample is shown in Figure 4.9 (a).

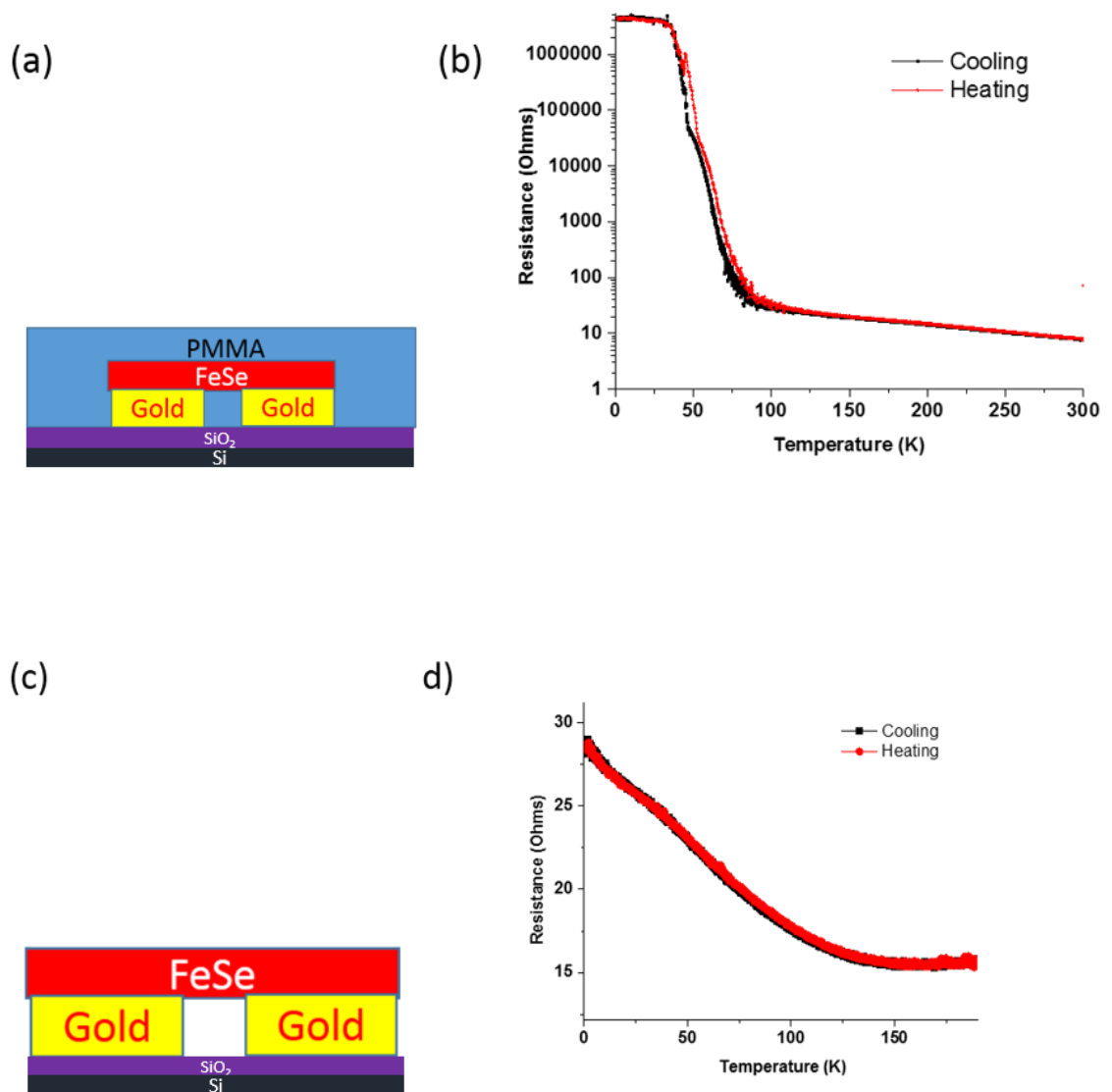


Figure 4.9 (a)Structural diagram of FeSe sample covered by PMMA (b) Temperature dependence of resistance for FeSe covered by PMMA (c) Structure of FeSe sample without PMMA (d) Temperature dependence of resistance for FeSe

Figure 4.9 (b) shows the temperature dependence of resistance for FeSe covered by PMMA, resistance increased dramatically when it was cooled to 77K. One of the possible explanations is that air was trapped under the gap below FeSe, when the temperature reached around 77K, the nitrogen gas in air condensed to liquid phase which resulted in a bad contact between electrodes and the FeSe. The condensation of the nitrogen gas

caused the pressure in the enclosed area to be decreased which resulted in the bending of the FeSe that caused a bad contact. At the end, the resistance increased significantly.

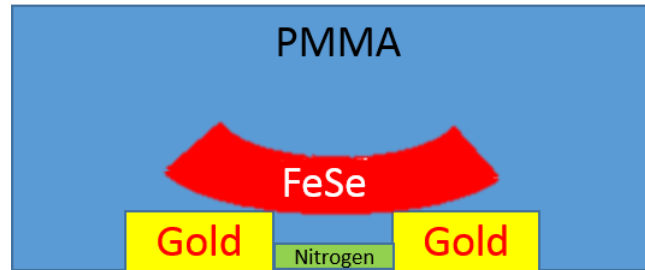


Figure 4.10 Bad contact for FeSe with gold electrodes below 77K

A further analysis was done to study this phenomena, another sample was prepared without the protective PMMA layer as shown in Figure 4.9(c). As the Figure 4.9(d) reveals, the resistance did not increase dramatically like the previous sample. On the other hand, when the temperature reached around 125K, the resistance increased steadily which showed a semiconductor behaviour. From Figure 4.9(d), no superconductivity could be observed as it is expected to observe a transition around 8K, which might be due to the contamination of sample to the environment.

4.4. Summary

In conclusion, Raman spectra of As_2S_3 were found to be same after the electrode preparation. This finding perhaps implies that electrode preparation does not have any structural influence on As_2S_3 , a low melting point material. I-V characteristics curve of MoS_2 , As_2S_3 and p-n junction, then, were measured under various circumstances such as low temperature and under LED white light. IV curves of As_2S_3 and p-n junction have shown a behaviour of high resistance which might due to the low hole mobility in As_2S_3 ($10^{-10} \text{ cm}^2/\text{Vs}$) [56]. The present of white light did increase the conductivity however the



increment is not very significant. Different transition behaviours were observed in FeTe samples. This phenomenon may be attributed to the different thicknesses of FeTe. As shown in optical images, Figure 4.8 (a), (c), (e), the colour contrast in these images might suggest that the difference in thickness. For FeSe sample, covering it by using PMMA has caused a bad contact which leads to drastically increase of its resistance. Lastly, none of the FeTe or FeSe samples on silicon substrate reveals the superconductivity behaviour.



5. Conclusion and Future Work

5.1. Conclusion

In conclusion, this thesis was an attempt to study the optical and electrical properties of 2D materials. Several experiments have been conducted in order to understand the fundamental properties of iron based 2D materials (FeTe, FeSe), As_2S_3 and MoS_2 . All key results and conclusions of these research works are summarized in this chapter.

Crystalline orientation and thickness identification of 2D materials are very important research topics due to the unique properties of 2D materials which making them a promising candidate for optic electronic and sensing devices. MoS_2 was encapsulated in between PMMA and SU-8, and modified bending technique was applied in different uniaxial strain directions to study the Raman respond of E_{2g}^1 and A_{1g} modes with respect to various strain directions. For bulk MoS_2 , the Raman shift rates of these two modes were insensitive to different direction of applied strains. On the other hand, the Raman shift rates of E_{2g}^1 and A_{1g} modes of few-layer MoS_2 were around $1.5 \text{ cm}^{-1}/\text{strain}$ with additional 60° applied to this angle, the Raman shift rates dropped to a small value. A possible explanation for this result is that originally the bending direction is along armchair direction after the additional 60° applied angle causes it changes from the armchair to zigzag direction. A facile technique can be used to identify the crystalline orientation direction of the few layer MoS_2 using the strained exfoliated MoS_2 and Raman spectroscopy based on the respond of E_{2g}^1 and A_{1g} modes with respect to different strain



directions. This method provides a way to explore the anisotropic strain-depend electrical and optical properties of MoS₂.

Secondly, Raman spectra of different thicknesses of exfoliated FeTe on top silicon substrate were also presented in this work. The vibrational modes A_{1g} and B_{1g} of FeTe were used to identify the thickness of exfoliated FeTe. This study has shown that the thickness of FeTe is correlated to its number of layers. This kind of changes is also observed in other 2D materials such as MoS₂. It is hoped that the present research has made a contribution to further study in FeTe and also provides evidence that Raman spectroscopy, can be a good tool to be use to confirm the thickness of FeTe if a clearer relationship can be established.

Thirdly, Raman spectra of exfoliated As₂S₃ on silicon substrate were also studied in this thesis in order to understand the influence of electrode preparation on 2D material with low melting temperature. Raman measurement was carried out after different electrode preparation processes. Raman spectra were found to be the same after each of the processes. Thus, we believe that electrode preparation does not bring any structural influences in 2D materials. Furthermore, exfoliated As₂S₃ was used to form p-n junction together with n-type MoS₂ which was transferred on top of As₂S₃ by using dry transferred method. I-V characteristic curve was obtained under various conditions in order to investigate the electrical properties of p-n junction. I-V curve of As₂S₃ and p-n junction showed a very low current conductivity. One of the possible reason is that the low hole mobility in As₂S₃ which leads to the low current conductivity.

Lastly, superconductivity behavior of FeSe and FeTe was studied in this work. Both materials were prepared in two different approaches which FeSe was dry transferred on top of electrodes but FeTe was mechanically exfoliated on silicon substrate then



electrodes were prepared on top of it. Only one of the samples showed a structural transition. However, none of the FeSe or FeTe shows the superconductivity behavior.

5.2. Future work

In this project, the most apparent limitation of the study lies in the number of samples are limited. A priority in future research would be to prepare more samples for FeTe and FeSe to obtain more data points. More studies are recommended to determine whether the relationship between Raman peak separation and its number of layers of FeTe sample and the same time, it would be interesting to discover whether the superconductivity behaviour of FeTe sample changes corresponding to its number of layers. Based on the finding of others regarding how the substrate effect on its superconductivity[85], there seems to be a need for the study of superconductivity of FeTe on different substrates like PMN-Pt, MgO or STO. At the meantime, it would be interesting to discover whether superconductivity of NbSe₂ varies to different substrates to learn about what is the relationship between its substrate and superconductivity. Since superconductivity of NbSe₂ on silicon substrate was fully studied [80], and it showed a promising result. Therefore, a further study can be conducted.

The modified bending technique in this thesis can also be used to investigate other electrical, optical or thermal property of other 2D materials which can bring a significant influence in fabrication of devices. A further study regard 2D family group in superconductor should also be done to full up the gap. For example, FeSe_{1-x}Te_x is a layered material that has a transition temperature at 11.8 K [116]. However, it is still a gap to be filled regard to the thickness dependence of this material.



Reference

- [1] K. S. Novoselov, A. K. Geim, S. V. Morozov, D. Jiang, Y. Zhang, S. V. Dubonos, *et al.*, "Electric Field Effect in Atomically Thin Carbon Films," *Science*, vol. 306, pp. 666-669, 2004.
- [2] C. Soldano, A. Mahmood, and E. Dujardin, "Production, properties and potential of graphene," *Carbon*, vol. 48, pp. 2127-2150, 7// 2010.
- [3] M. J. Allen, V. C. Tung, and R. B. Kaner, "Honeycomb Carbon: A Review of Graphene," *Chemical Reviews*, vol. 110, pp. 132-145, 2010/01/13 2010.
- [4] N. Van Tu, L. Huu Doan, N. Van Chuc, Tam N. Thi Thanh, L. Dinh Quang, N. Xuan Nghia, *et al.*, "Synthesis of multi-layer graphene films on copper tape by atmospheric pressure chemical vapor deposition method," *Advances in Natural Sciences: Nanoscience and Nanotechnology*, vol. 4, p. 035012, 2013.
- [5] Q. H. Wang, K. Kalantar-Zadeh, A. Kis, J. N. Coleman, and M. S. Strano, "Electronics and optoelectronics of two-dimensional transition metal dichalcogenides," *Nat Nano*, vol. 7, pp. 699-712, 11//print 2012.
- [6] M. Fontana, T. Deppe, A. K. Boyd, M. Rinzan, A. Y. Liu, M. Paranjape, *et al.*, "Electron-hole transport and photovoltaic effect in gated MoS₂ Schottky junctions," *Scientific Reports*, vol. 3, p. 1634, 04/09/online 2013.
- [7] P. Joensen, Frindt, R.F. & Morrison, S.R., "Single layer MoS₂ " *Mater.Res.Bull* vol. 21, pp. 457-461, 1986.
- [8] J. Zheng, H. Zhang, S. Dong, Y. Liu, C. Tai Nai, H. Suk Shin, *et al.*, "High yield exfoliation of two-dimensional chalcogenides using sodium naphthalenide," *Nature Communications*, vol. 5, p. 2995, 01/02/online 2014.
- [9] K. F. Mak, K. He, C. Lee, G. H. Lee, J. Hone, T. F. Heinz, *et al.*, "Tightly bound trions in monolayer MoS₂," *Nat Mater*, vol. 12, pp. 207-211, 03//print 2013.
- [10] C. Huang, S. Wu, A. M. Sanchez, J. J. P. Peters, R. Beanland, J. S. Ross, *et al.*, "Lateral heterojunctions within monolayer MoSe₂-WSe₂ semiconductors," *Nat Mater*, vol. 13, pp. 1096-1101, 12//print 2014.
- [11] A. Berkdemir, H. R. Gutiérrez, A. R. Botello-Méndez, N. Perea-López, A. L. Elías, C.-I. Chia, *et al.*, "Identification of individual and few layers of WS(2) using Raman Spectroscopy," *Scientific Reports*, vol. 3, p. 1755, 04/15/ 2013.
- [12] J. Kang, W. Cao, X. Xie, D. Sarkar, W. Liu, and K. Banerjee, "Graphene and beyond-graphene 2D crystals for next-generation green electronics," 2014, pp. 908305-908305-7.
- [13] N. Liu, P. Kim, J. H. Kim, J. H. Ye, S. Kim, and C. J. Lee, "Large-Area Atomically Thin MoS₂ Nanosheets Prepared Using Electrochemical Exfoliation," *ACS Nano*, vol. 8, pp. 6902-6910, 2014/07/22 2014.
- [14] V. Nicolosi, M. Chhowalla, M. G. Kanatzidis, M. S. Strano, and J. N. Coleman, "Liquid Exfoliation of Layered Materials," *Science*, vol. 340, 2013.
- [15] Y.-H. Lee, X.-Q. Zhang, W. Zhang, M.-T. Chang, C.-T. Lin, K.-D. Chang, *et al.*, "Synthesis of Large-Area MoS₂ Atomic Layers with Chemical Vapor Deposition," *Advanced Materials*, vol. 24, pp. 2320-2325, 2012.
- [16] Y. Zhan, Z. Liu, S. Najmaei, P. M. Ajayan, and J. Lou, "Large-Area Vapor-Phase Growth and Characterization of MoS₂ Atomic Layers on a SiO₂ Substrate," *Small*, vol. 8, pp. 966-971, 2012.



- [17] O. Lopez-Sanchez, D. Lembke, M. Kayci, A. Radenovic, and A. Kis, "Ultrasensitive photodetectors based on monolayer MoS₂," *Nat Nano*, vol. 8, pp. 497-501, 07//print 2013.
- [18] G. Eda, H. Yamaguchi, D. Voiry, T. Fujita, M. Chen, and M. Chhowalla, "Photoluminescence from Chemically Exfoliated MoS₂," *Nano Letters*, vol. 11, pp. 5111-5116, 2011/12/14 2011.
- [19] K. S. Novoselov, D. Jiang, F. Schedin, T. J. Booth, V. V. Khotkevich, S. V. Morozov, *et al.*, "Two-dimensional atomic crystals," *Proceedings of the National Academy of Sciences of the United States of America*, vol. 102, pp. 10451-10453, July 26, 2005 2005.
- [20] K. F. Mak, C. Lee, J. Hone, J. Shan, and T. F. Heinz, "Atomically Thin MoS_2 : A New Direct-Gap Semiconductor," *Physical Review Letters*, vol. 105, p. 136805, 09/24/ 2010.
- [21] M. M. Benameur, B. Radisavljevic, J. S. Héron, S. Sahoo, H. Berger, and A. Kis, "Visibility of dichalcogenide nanolayers," *Nanotechnology*, vol. 22, p. 125706, 2011.
- [22] RadisavljevicB, RadenovicA, BrivioJ, GiacomettiV, and KisA, "Single-layer MoS₂ transistors," *Nat Nano*, vol. 6, pp. 147-150, 03//print 2011.
- [23] X. Xi, L. Zhao, Z. Wang, H. Berger, L. Forró, J. Shan, *et al.*, "Strongly enhanced charge-density-wave order in monolayer NbSe₂," *Nat Nano*, vol. 10, pp. 765-769, 09//print 2015.
- [24] K. M. F. Shahil, M. Z. Hossain, D. Teweldebrhan, and A. A. Balandin, "Crystal symmetry breaking in few-quintuple Bi₂Te₃ films: Applications in nanometrology of topological insulators," *Applied Physics Letters*, vol. 96, p. 153103, 2010.
- [25] Z. Zeng, Z. Yin, X. Huang, H. Li, Q. He, G. Lu, *et al.*, "Single-Layer Semiconducting Nanosheets: High-Yield Preparation and Device Fabrication," *Angewandte Chemie International Edition*, vol. 50, pp. 11093-11097, 2011.
- [26] H. Li, G. Lu, Z. Yin, Q. He, H. Li, Q. Zhang, *et al.*, "Optical Identification of Single- and Few-Layer MoS₂ Sheets," *Small*, vol. 8, pp. 682-686, 2012.
- [27] J. Zhang, Z. Peng, A. Soni, Y. Zhao, Y. Xiong, B. Peng, *et al.*, "Raman Spectroscopy of Few-Quintuple Layer Topological Insulator Bi₂Se₃ Nanoplatelets," *Nano Letters*, vol. 11, pp. 2407-2414, 2011/06/08 2011.
- [28] Y. Shen, F. e. Chen, P. Wu, and G. Shi, "A two-dimensional Raman spectroscopic study on the structural changes of a polythiophene film during the cooling process," *The Journal of Chemical Physics*, vol. 119, pp. 11415-11419, 2003.
- [29] H. Takahashi, K. Igawa, K. Arii, Y. Kamihara, M. Hirano, and H. Hosono, "Superconductivity at 43 K in an iron-based layered compound LaO_{1-x}F_xFeAs," *Nature*, vol. 453, pp. 376-378, 05/15/print 2008.
- [30] C. A. Reynolds, B. Serin, and L. B. Nesbitt, "The Isotope Effect in Superconductivity. I. Mercury," *Physical Review*, vol. 84, pp. 691-694, 11/15/ 1951.
- [31] Y. Kamihara, T. Watanabe, M. Hirano, and H. Hosono, "Iron-Based Layered Superconductor La[O_{1-x}F_x]FeAs (x = 0.05–0.12) with T_c = 26 K," *Journal of the American Chemical Society*, vol. 130, pp. 3296-3297, 2008/03/01 2008.
- [32] Z.-A. Ren, W. Lu, J. Yang, W. Yi, X.-L. Shen, C. Zheng, *et al.*, "Superconductivity at 55 K in Iron-Based F-Doped Layered Quaternary Compound Sm[O_{1-x}F_x]FeAs," *Chinese Physics Letters*, vol. 25, p. 2215, 2008.



- [33] Y. F. Nie, D. Telesca, J. I. Budnick, B. Sinkovic, and B. O. Wells, "Superconductivity induced in iron telluride films by low-temperature oxygen incorporation," *Physical Review B*, vol. 82, p. 020508, 07/19/ 2010.
- [34] "Superconductivity under High Pressure in LaFeAsO," *Journal of the Physical Society of Japan*, vol. 77, p. 113712, 2008/11/15 2008.
- [35] M. Gooch, B. Lv, J. H. Tapp, Z. Tang, B. Lorenz, A. M. Guloy, *et al.*, "Pressure shift of the superconducting T_c of LiFeAs," *EPL (Europhysics Letters)*, vol. 85, p. 27005, 2009.
- [36] D. Jariwala, V. K. Sangwan, L. J. Lauhon, T. J. Marks, and M. C. Hersam, "Emerging Device Applications for Semiconducting Two-Dimensional Transition Metal Dichalcogenides," *ACS Nano*, vol. 8, pp. 1102-1120, 2014/02/25 2014.
- [37] G. Eda, H. Yamaguchi, D. Voiry, T. Fujita, M. Chen, and M. Chhowalla, "Correction to Photoluminescence from Chemically Exfoliated MoS₂," *Nano Letters*, vol. 12, pp. 526-526, 2012/01/11 2012.
- [38] D. Akinwande, N. Petrone, and J. Hone, "Two-dimensional flexible nanoelectronics," *Nature Communications*, vol. 5, p. 5678, 12/17/online 2014.
- [39] X. Li and H. Zhu, "Two-dimensional MoS₂: Properties, preparation, and applications," *Journal of Materiomics*, vol. 1, pp. 33-44, 3// 2015.
- [40] B. Ryan, C. Luiz Gustavo, and N. Lukas, "Raman characterization of defects and dopants in graphene," *Journal of Physics: Condensed Matter*, vol. 27, p. 083002, 2015.
- [41] C. Lee, H. Yan, L. E. Brus, T. F. Heinz, J. Hone, and S. Ryu, "Anomalous Lattice Vibrations of Single- and Few-Layer MoS₂," *ACS Nano*, vol. 4, pp. 2695-2700, 2010/05/25 2010.
- [42] H. Li, Q. Zhang, C. C. R. Yap, B. K. Tay, T. H. T. Edwin, A. Olivier, *et al.*, "From Bulk to Monolayer MoS₂: Evolution of Raman Scattering," *Advanced Functional Materials*, vol. 22, pp. 1385-1390, 2012.
- [43] A. Splendiani, L. Sun, Y. Zhang, T. Li, J. Kim, C.-Y. Chim, *et al.*, "Emerging Photoluminescence in Monolayer MoS₂," *Nano Letters*, vol. 10, pp. 1271-1275, 2010/04/14 2010.
- [44] K. Dolui, I. Rungger, and S. Sanvito, "Origin of the n -type and p -type conductivity of MoS₂ monolayers on a SiO₂ substrate," *Physical Review B*, vol. 87, p. 165402, 04/02/ 2013.
- [45] Z. Yin, H. Li, H. Li, L. Jiang, Y. Shi, Y. Sun, *et al.*, "Single-Layer MoS₂ Phototransistors," *ACS Nano*, vol. 6, pp. 74-80, 2012/01/24 2012.
- [46] F.-C. Hsu, J.-Y. Luo, K.-W. Yeh, T.-K. Chen, T.-W. Huang, P. M. Wu, *et al.*, "Superconductivity in the PbO-type structure α -FeSe," *Proceedings of the National Academy of Sciences*, vol. 105, pp. 14262-14264, September 23, 2008 2008.
- [47] Y. M. Y. Takano, "Review of Fe Chalcogenides as the Simplest Fe-Based Superconductor," *Journal of the Physical Society of Japan*, vol. 79, p. 102001, 2010/10/15 2010.
- [48] H. Nohara H. Kotegawa Y. Hara H. Tou Y. Mizuguchi Y. Takano, "RF Surface Impedance and ⁷⁷Se-NMR Studies of FeSe: Effect of the Sample Quality," *Journal of the Physical Society of Japan*, vol. 80, p. SA120, 2011/01/02 2011.
- [49] Y. Mizuguchi, F. Tomioka, S. Tsuda, T. Yamaguchi, and Y. Takano, "FeTe as a candidate material for new iron-based superconductor," *Physica C: Superconductivity*, vol. 469, pp. 1027-1029, 10/15/ 2009.



- [50] M. H. Fang, H. M. Pham, B. Qian, T. J. Liu, E. K. Vehstedt, Y. Liu, *et al.*, "Superconductivity close to magnetic instability in $\text{Fe}_{1-x}\text{Se}_x\text{Te}_{0.82}$," *Physical Review B*, vol. 78, p. 224503, 12/03/ 2008.
- [51] Y. Mizuguchi, F. Tomioka, S. Tsuda, T. Yamaguchi, and Y. Takano, "Superconductivity in S-substituted FeTe," *Applied Physics Letters*, vol. 94, p. 012503, 2009.
- [52] F. Ma, W. Ji, J. Hu, Z.-Y. Lu, and T. Xiang, "First-Principles Calculations of the Electronic Structure of Tetragonal α -FeTe and α -FeSe Crystals: Evidence for a Bicollinear Antiferromagnetic Order," *Physical Review Letters*, vol. 102, p. 177003, 04/29/ 2009.
- [53] E. Färm, M. J. Heikkilä, M. Vehkamäki, K. Mizohata, M. Ritala, M. Leskelä, *et al.*, "As₂S₃ thin films deposited by atomic layer deposition," *Journal of Vacuum Science & Technology A: Vacuum, Surfaces, and Films*, vol. 35, p. 01B114, 2017.
- [54] D. J. Plazek and K. L. Ngai, "The Glass Temperature," in *Physical Properties of Polymers Handbook*, J. E. Mark, Ed., ed New York, NY: Springer New York, 2007, pp. 187-215.
- [55] K. Tanaka and H. Hisakuni, "Photoinduced phenomena in As₂S₃ glass under sub-bandgap excitation," *Journal of Non-Crystalline Solids*, vol. 198, pp. 714-718, 1996/05/02 1996.
- [56] I. P. C. A. M. Andriesh, P. J. S. Ewen, A. E. Owen and a, "EVALUATION OF HOLE DRIFT MOBILITY IN GLASSY As₂S₃ IN THE TEMPERATURE RANGE 77 - 330 K," *Journal of Optoelectronics and Advanced Materials* vol. 3, pp. 27-31, 2001.
- [57] G. Yang, B. Bureau, T. Rouxel, Y. Gueguen, O. Gulbiten, C. Roiland, *et al.*, "Correlation between structure and physical properties of chalcogenide glasses in the $\text{As}_x\text{Se}_{1-x}$ system," *Physical Review B*, vol. 82, p. 195206, 11/17/ 2010.
- [58] Y. Kato, R. C. Myers, A. C. Gossard, and D. D. Awschalom, "Coherent spin manipulation without magnetic fields in strained semiconductors," *Nature*, vol. 427, pp. 50-53, 01/01/print 2004.
- [59] X. Xu, W. Yao, D. Xiao, and T. F. Heinz, "Spin and pseudospins in layered transition metal dichalcogenides," *Nat Phys*, vol. 10, pp. 343-350, 05//print 2014.
- [60] C. Pan, L. Dong, G. Zhu, S. Niu, R. Yu, Q. Yang, *et al.*, "High-resolution electroluminescent imaging of pressure distribution using a piezoelectric nanowire LED array," *Nat Photon*, vol. 7, pp. 752-758, 09//print 2013.
- [61] C. Lee, X. Wei, J. W. Kysar, and J. Hone, "Measurement of the Elastic Properties and Intrinsic Strength of Monolayer Graphene," *Science*, vol. 321, pp. 385-388, 2008.
- [62] P. Lu, X. Wu, W. Guo, and X. C. Zeng, "Strain-dependent electronic and magnetic properties of MoS₂ monolayer, bilayer, nanoribbons and nanotubes," *Physical Chemistry Chemical Physics*, vol. 14, pp. 13035-13040, 2012.
- [63] Y. Y. Hui, X. Liu, W. Jie, N. Y. Chan, J. Hao, Y.-T. Hsu, *et al.*, "Exceptional Tunability of Band Energy in a Compressively Strained Trilayer MoS₂ Sheet," *ACS Nano*, vol. 7, pp. 7126-7131, 2013/08/27 2013.
- [64] K. He, C. Poole, K. F. Mak, and J. Shan, "Experimental Demonstration of Continuous Electronic Structure Tuning via Strain in Atomically Thin MoS₂," *Nano Letters*, vol. 13, pp. 2931-2936, 2013/06/12 2013.



- [65] S. M. S. a. K. K. Ng, *Physics of semiconductor Devices*, 3rd edn ed.: Wiley, 2006.
- [66] H. Fang, C. Battaglia, C. Carraro, S. Nemsak, B. Ozdol, J. S. Kang, *et al.*, "Strong interlayer coupling in van der Waals heterostructures built from single-layer chalcogenides," *Proceedings of the National Academy of Sciences*, vol. 111, pp. 6198-6202, April 29, 2014 2014.
- [67] P. Woanseo, P. Juhun, J. Jingon, L. Hyungwoo, J. Hyunhak, C. Kyungjune, *et al.*, "Oxygen environmental and passivation effects on molybdenum disulfide field effect transistors," *Nanotechnology*, vol. 24, p. 095202, 2013.
- [68] C.-H. Lee, G.-H. Lee, A. M. van der Zande, W. Chen, Y. Li, M. Han, *et al.*, "Atomically thin p–n junctions with van der Waals heterointerfaces," *Nat Nano*, vol. 9, pp. 676-681, 09//print 2014.
- [69] T. Roy, M. Tosun, J. S. Kang, A. B. Sachid, S. B. Desai, M. Hettick, *et al.*, "Field-Effect Transistors Built from All Two-Dimensional Material Components," *ACS Nano*, vol. 8, pp. 6259-6264, 2014/06/24 2014.
- [70] M.-L. Tsai, S.-H. Su, J.-K. Chang, D.-S. Tsai, C.-H. Chen, C.-I. Wu, *et al.*, "Monolayer MoS₂ Heterojunction Solar Cells," *ACS Nano*, vol. 8, pp. 8317-8322, 2014/08/26 2014.
- [71] "Facile fabrication of a ultraviolet tunable MoS₂/p-Si junction diode," *Applied Physics Letters*, vol. 106, p. 193504, 2015/05/11 2015.
- [72] Y. Deng, Z. Luo, N. J. Conrad, H. Liu, Y. Gong, S. Najmaei, *et al.*, "Black Phosphorus–Monolayer MoS₂ van der Waals Heterojunction p–n Diode," *ACS Nano*, vol. 8, pp. 8292-8299, 2014/08/26 2014.
- [73] A. Jongtae, J. Pyo Jin, R. Syed Raza Ali, P. Atiye, M. Sung-Wook, H. Do Kyung, *et al.*, "Transition metal dichalcogenide heterojunction PN diode toward ultimate photovoltaic benefits," *2D Materials*, vol. 3, p. 045011, 2016.
- [74] A. Pezeshki, S. H. H. Shokouh, T. Nazari, K. Oh, and S. Im, "Electric and Photovoltaic Behavior of a Few-Layer α -MoTe₂/MoS₂ Dichalcogenide Heterojunction," *Advanced Materials*, vol. 28, pp. 3216-3222, 2016.
- [75] W. Serrano, N. J. Pinto, C. H. Naylor, N. J. Kybert, and A. T. C. J. Jr., "Facile fabrication of a ultraviolet tunable MoS₂/p-Si junction diode," *Applied Physics Letters*, vol. 106, p. 193504, 2015.
- [76] R. Cheng, D. Li, H. Zhou, C. Wang, A. Yin, S. Jiang, *et al.*, "Electroluminescence and Photocurrent Generation from Atomically Sharp WSe₂/MoS₂ Heterojunction p–n Diodes," *Nano Letters*, vol. 14, pp. 5590-5597, 2014/10/08 2014.
- [77] M. M. Furchi, A. Pospischil, F. Libisch, J. Burgdörfer, and T. Mueller, "Photovoltaic Effect in an Electrically Tunable van der Waals Heterojunction," *Nano Letters*, vol. 14, pp. 4785-4791, 2014/08/13 2014.
- [78] D. Costanzo, S. Jo, H. Berger, and A. F. Morpurgo, "Gate-induced superconductivity in atomically thin MoS₂ crystals," *Nat Nano*, vol. 11, pp. 339-344, 04//print 2016.
- [79] R. F. Frindt, "Superconductivity in Ultrathin NbSe₂ Layers," *Physical Review Letters*, vol. 28, pp. 299-301, 01/31/ 1972.
- [80] X. Xi, Z. Wang, W. Zhao, J.-H. Park, K. T. Law, H. Berger, *et al.*, "Ising pairing in superconducting NbSe₂ atomic layers," *Nat Phys*, vol. 12, pp. 139-143, 02//print 2016.
- [81] M. Burrard-Lucas, D. G. Free, S. J. Sedlmaier, J. D. Wright, S. J. Cassidy, Y. Hara, *et al.*, "Enhancement of the superconducting transition temperature of FeSe by intercalation of a molecular spacer layer," *Nat Mater*, vol. 12, pp. 15-19, 01//print 2013.



- [82] S. Medvedev, T. M. McQueen, I. A. Troyan, T. Palasyuk, M. I. Eremets, R. J. Cava, *et al.*, "Electronic and magnetic phase diagram of [beta]-Fe_{1.01}Se with superconductivity at 36.7 K under pressure," *Nat Mater*, vol. 8, pp. 630-633, 08/print 2009.
- [83] J.-F. Ge, Z.-L. Liu, C. Liu, C.-L. Gao, D. Qian, Q.-K. Xue, *et al.*, "Superconductivity above 100 K in single-layer FeSe films on doped SrTiO₃," *Nat Mater*, vol. 14, pp. 285-289, 03/print 2015.
- [84] D.-x. Mou, L. Zhao, and X.-j. Zhou, "Structural, magnetic and electronic properties of the iron-chalcogenide A_xFe_{2-y}Se₂ (A=K, Cs, Rb, and Tl, etc.) superconductors," *Frontiers of Physics*, vol. 6, pp. 410-428, 2011.
- [85] Y. Han, W. Y. Li, L. X. Cao, X. Y. Wang, B. Xu, B. R. Zhao, *et al.*, "Superconductivity in Iron Telluride Thin Films under Tensile Stress," *Physical Review Letters*, vol. 104, p. 017003, 01/08/ 2010.
- [86] R. H. Dale, T. F. Anthony, and D. D. John, "Theory of high- T_C superconductivity: transition temperature," *Journal of Physics: Condensed Matter*, vol. 23, p. 295701, 2011.
- [87] A. Castellanos-Gomez, R. Roldán, E. Cappelluti, M. Buscema, F. Guinea, H. S. J. van der Zant, *et al.*, "Local Strain Engineering in Atomically Thin MoS₂," *Nano Letters*, vol. 13, pp. 5361-5366, 2013/11/13 2013.
- [88] Y. A. Koksharov, "Magnetism of Nanoparticles: Effects of Size, Shape, and Interactions," in *Magnetic Nanoparticles*, ed: Wiley-VCH Verlag GmbH & Co. KGaA, 2009, pp. 197-254.
- [89] E. Alfonso, G. Cubillos, and J. Olaya, *Thin Film Growth Through Sputtering Technique and Its Applications*: INTECH Open Access Publisher, 2012.
- [90] M. E. S.Arula, M. meikandan, "Different Types Of PVD Coatings and their Demands – A Review," *International Journal of Applied Engineering Research*, vol. 9, Number 24, pp. pp. 26417-26430, 2014.
- [91] K. S. Sree Harsha, "Chapter 6 - Gas Flow in Thin Film Processing Systems," in *Principles of Vapor Deposition of Thin Films*, ed Oxford: Elsevier, 2006, pp. 453-533.
- [92] P. K. S. K. S. S. Harsha, *Principles of Vapor Deposition of Thin Films*: Elsevier Science, 2005.
- [93] N. S. Xu and S. E. Huq, "Novel cold cathode materials and applications," *Materials Science and Engineering: R: Reports*, vol. 48, pp. 47-189, 1/31/ 2005.
- [94] M. Yi and Z. Shen, "A review on mechanical exfoliation for the scalable production of graphene," *Journal of Materials Chemistry A*, vol. 3, pp. 11700-11715, 2015.
- [95] C.-G. Andres, B. Michele, M. Rianda, S. Vibhor, J. Laurens, S. J. v. d. Z. Herre, *et al.*, "Deterministic transfer of two-dimensional materials by all-dry viscoelastic stamping," *2D Materials*, vol. 1, p. 011002, 2014.
- [96] R. N. A. Jagtap, A H, "Overview literature on atomic force microscopy (AFM): Basics and its important applications for polymer characterization," *Indian Journal of Engineering and Materials Sciences (IJEMS)* vol. IJEMS Vol.13 [2006], Aug-2006.
- [97] D. V. Petrov, "Pressure dependence of peak positions, half widths, and peak intensities of methane Raman bands (ν_2 , $2\nu_4$, ν_1 , ν_3 , and $2\nu_2$)," *Journal of Raman Spectroscopy*, pp. n/a-n/a, 2017.
- [98] C. C. Moura, R. S. Tare, R. O. C. Oreffo, and S. Mahajan, "Raman spectroscopy and coherent anti-Stokes Raman scattering imaging: prospective tools for



- monitoring skeletal cells and skeletal regeneration," *Journal of The Royal Society Interface*, vol. 13, 2016.
- [99] C. V. Raman and K. S. Krishnan, "A New Type of Secondary Radiation," *Nature*, vol. 121, pp. 501-502, // 1928.
- [100] T. O. S. Colm, "Ohm's law and the definition of resistance," *Physics Education*, vol. 15, p. 237, 1980.
- [101] K. Jaewook, Y. U. Nam, M. Lampert, and Y. C. Ghim, "Reliability of the two-point measurement of the spatial correlation length from Gaussian-shaped fluctuating signals in fusion-grade plasmas," *Nuclear Fusion*, vol. 56, p. 106016, 2016.
- [102] C. Wooyeol and K. O. Kenneth, "Kelvin inductance and resistance measurements using an AC source and DC voltmeters," in *2016 IEEE MTT-S International Microwave Symposium (IMS)*, 2016, pp. 1-4.
- [103] W. M. Loh, K. Saraswat, and R. W. Dutton, "Analysis and scaling of Kelvin resistors for extraction of specific contact resistivity," *IEEE Electron Device Letters*, vol. 6, pp. 105-108, 1985.
- [104] N. Mainusch, T. Christ, T. Siedenbug, T. O'Donnell, M. Lutansieto, P.-J. Brand, *et al.*, "New Contact Probe and Method to Measure Electrical Resistances in Battery Electrodes," *Energy Technology*, vol. 4, pp. 1550-1557, 2016.
- [105] S. Yoshimoto, Y. Murata, K. Kubo, K. Tomita, K. Motoyoshi, T. Kimura, *et al.*, "Four-Point Probe Resistance Measurements Using PtIr-Coated Carbon Nanotube Tips," *Nano Letters*, vol. 7, pp. 956-959, 2007/04/01 2007.
- [106] G. Tsoukleri, J. Parthenios, K. Papagelis, R. Jalil, A. C. Ferrari, A. K. Geim, *et al.*, "Subjecting a Graphene Monolayer to Tension and Compression," *Small*, vol. 5, pp. 2397-2402, 2009.
- [107] C. Casiraghi, A. Hartschuh, E. Lidorikis, H. Qian, H. Harutyunyan, T. Gokus, *et al.*, "Rayleigh Imaging of Graphene and Graphene Layers," *Nano Letters*, vol. 7, pp. 2711-2717, 2007/09/01 2007.
- [108] C. Rice, R. J. Young, R. Zan, U. Bangert, D. Wolverson, T. Georgiou, *et al.*, "Raman-scattering measurements and first-principles calculations of strain-induced phonon shifts in monolayer MoS₂," *Physical Review B*, vol. 87, p. 081307, 02/15/ 2013.
- [109] C. Cong, J. Shang, X. Wu, B. Cao, N. Peimyoo, C. Qiu, *et al.*, "Synthesis and Optical Properties of Large-Area Single-Crystalline 2D Semiconductor WS₂ Monolayer from Chemical Vapor Deposition," *Advanced Optical Materials*, vol. 2, pp. 131-136, 2014.
- [110] A. Arab and Q. Li, "Anisotropic thermoelectric behavior in armchair and zigzag mono- and fewlayer MoS₂ in thermoelectric generator applications," *Scientific Reports*, vol. 5, p. 13706, 09/03/online 2015.
- [111] A. Berkdemir, H. R. Gutiérrez, A. R. Botello-Méndez, N. Perea-López, A. L. Elías, C.-I. Chia, *et al.*, "Identification of individual and few layers of WS₂ using Raman Spectroscopy," *Scientific Reports*, vol. 3, p. 1755, 04/30/online 2013.
- [112] T. R. Groves, "Theory of beam-induced substrate heating," *Journal of Vacuum Science & Technology B: Microelectronics and Nanometer Structures Processing, Measurement, and Phenomena*, vol. 14, pp. 3839-3844, 1996.
- [113] C. Rice, R.J. Young, "Raman analysis of laser-processed glass materials," *Glass 01*, Oct 24 2013.
- [114] J. Devrees, *Recent Developments in Condensed Matter Physics: Volume 2 · Metals, Disordered Systems, Surfaces, and Interfaces*: Springer US, 2012.



- [115] A. J. Williams, T. M. McQueen, V. Ksenofontov, C. Felser, and R. J. Cava, "The metal–insulator transition in Fe_{1.01–x}Cu_xSe," *Journal of Physics: Condensed Matter*, vol. 21, p. 305701, 2009.
- [116] H. Nohara H. Kotegawa Y. Hara H. Tou Y. Mizuguchi Y. Takano, "Substitution Effects on FeSe Superconductor," *Journal of the Physical Society of Japan*, vol. 78, p. 074712, 2009/07/15 2009.